Research on spatiotemporal distribution measurement of odor trace with localized surface plasmon resonance gas sensor

楊, 中元

Research on spatiotemporal distribution measurement of odor trace with localized surface plasmon resonance gas sensor

Zhongyuan Yang

Graduate School of Information Science and Electrical Engineering
Kyushu University

January 2024

Contents

Figures list

Chapter 1

Chapter 2

Chapter 3

Chapter 4

Chapter 5

Symbols and abbreviations

A	absorbance	
I	Incident light	
R	Reflected light	
S	Scattered light	
T	Transmitted light	
T	Transmittance	%
∆T	Transmittance variation	%

AuNPs	Au nanoparticles
AgNPs	Ag nanoparticles
CCD	Charge-coupled Device
LED	Light emitting diode
LSPR	Localized surface plasmon resonance
MIP	Molecular imprinted polymer
PID	Photoionization detector
PMMA	Poly methyl methacrylate
PP	Polypropylene
QCM	Quartz crystal microbalance
SEM	Scanning electron microscope
VOC	Volatile organic compound

Chapter 1 Introduction

1.1 Odor information

Chemical substances which can deliver a large amount of invisible information are used by many creatures with olfactory senses for cognition, exploration, crisis management, and communication. The human olfactory system detects various gas molecules in the air, leading us to perceive different odors (1,2). Generally, what we refer to as ‘smelling’ is actually the detection of specific gaseous chemical substances associated with an odor. The study of "Odor sensor" to reproduce the olfactory sense of living things is more complicated than the other four senses that are more easily quantified because there is no primary sense of smell (3). In addition, there are hundreds of thousands of substances that produce odors, which greatly increases the difficulty of classifying odor substances (4). Odor information, which is the combination of volatile chemical mixture components, potentially contains a vast amount of information. Odor information is divided into three aspects in this research: type, concentration, and spatial distribution.

Type of odor information: Identifying the type of odor substance is fundamental in many scientific fields. In environmental science, distinguishing natural odors from pollutants helps in assessing air quality and identifying sources of contamination. In the food industry, recognizing specific odors is essential for quality control, as it can indicate freshness or spoilage of products. In medical diagnostics, certain diseases emit characteristic odors; for instance, the sweet smell of acetone in breath can indicate diabetes (5). Thus, understanding type of odor substance is crucial for environmental monitoring, food safety, and health diagnostics.

Concentration of odor information: The concentration of odor information is also important in human daily life. In environmental monitoring, the concentration of certain chemicals in the air can signal the presence and severity of pollution. High concentrations of harmful gases like sulfur dioxide or ammonia can have dire health and ecological consequences (6). In the perfume industry, the concentration determines the strength and longevity of a fragrance. In occupational health, monitoring the concentration of volatile organic compounds in workplaces is critical to ensure worker safety. Therefore, measuring and analyzing odor concentration is vital for environmental protection, product formulation, and health and safety regulations.

Spatial distribution of odor information: The spatial distribution of odor information provides invaluable insights across several areas. In urban planning, mapping odor

sources helps in designing cities that minimize residents' exposure to unpleasant smells. In ecology, understanding how odors disperse in an environment can reveal animal behavior patterns, such as how predators track prey or how plants attract pollinators (7). In disaster response, mapping the spread of chemical odors can guide evacuation and containment strategies (8). Consequently, the spatial distribution analysis of odor information is essential for urban development, ecological research, and emergency management.

Particularly, unlike sound waves or light, odor information has the unique feature of adhering to the site and recording past events (9). The identification of things through gaseous substances via volatile chemical substances, is promising in terms of non-contact, non-destructive, and remote detection through obstacles. Leading with optical imaging sensors and accelerometers, physical sensor systems connected to computers have become indispensable technologies in modern society. On the other hand, the use of chemical sensors for detecting chemical substances is still under development. To extensively utilize this "odor information," it often relies on specially trained animals in many cases. In various commercial applications and disaster rescue operations, the olfactory system of dogs remains the most advanced detection and identification system. The development of artificial olfactory systems, which could reduce the significant time and cost required for acquisition and training, is a challenging task from scientific and industrial perspectives. However, even with a powerful olfactory system like a dog, its spatial resolution is limited to about 10 cm around the nose, and it does not obtain visual shape of distribution information. To capture the spatial distribution of odor traces, existing gas sensors used in spatial scanning with mobile robot lack the speed of information acquisition and spatial resolution, and the visualization measurement of odor trace itself has not been realized.

1.2 Gas detection methods

Gas sensors play an indispensable role in the field of odor/gas detection (10-13). In this section, mechanism of gas sensors, which are capable of gathering spatial distribution data of odors using mobile robots, will be introduced.

1.2.1 Semiconductor gas sensor

Semiconductor gas sensor is the most widely used gas sensor. The structure of semiconductor gas sensor is shown in Figure 1.1. Gas molecules adsorbed on the surface of semiconductors undergo chemical reactions with the semiconductor material. These reactions cause changes in the conductivity (resistance) of the semiconductor material.

For reducing gases (such as carbon monoxide and hydrogen), these gas molecules capture oxygen ions on the semiconductor surface, thereby reducing the number of carriers and increasing the material's resistance. For oxidizing gases (such as nitrogen oxides), additional carriers are released, lowering the resistance (14,15). Furthermore, the resistance change is related to the target gas concentration, so the target gas concentration can be calculated by measuring the change in resistance. Although the semiconductor gas sensor has a high sensitivity, but the low response speed will still be a limit for high-speed sensing and its lack of selectivity and high operating temperature are also not suitable for complex environment (16).

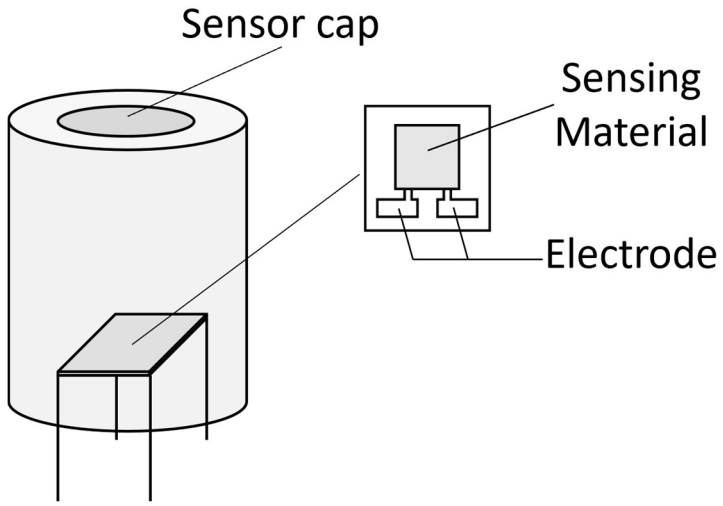

Figure 1. 1 Schematic diagram of semiconductor gas sensor.

1.2.2 Quartz Crystal Microbalance gas sensor

A schematic diagram of a typical Quartz Crystal Microbalance (QCM) based gas sensor is shown in Figure 1.3. Based on the sensitivity of the piezoelectric quartz substrate to the mass change, the target gas absorbed by the sensing film deposited on the electrode will change the frequency of quartz substrate and can realized the detection of target gas (17). The selectivity of QCM gas sensor can be controlled by the sensing film on the electrode or the electrodes themselves can be made of a material which is selective to target analytes (18, 19). However, there is a disadvantage that it is necessary to wait for desorption of adsorbed molecules after adsorption and detection, so it cannot be used for measurement of gas concentration change in a short time. Moreover, QCM sensor is easily affected by environmental changes (such as temperature, humidity, and pressure) and relatively high price.

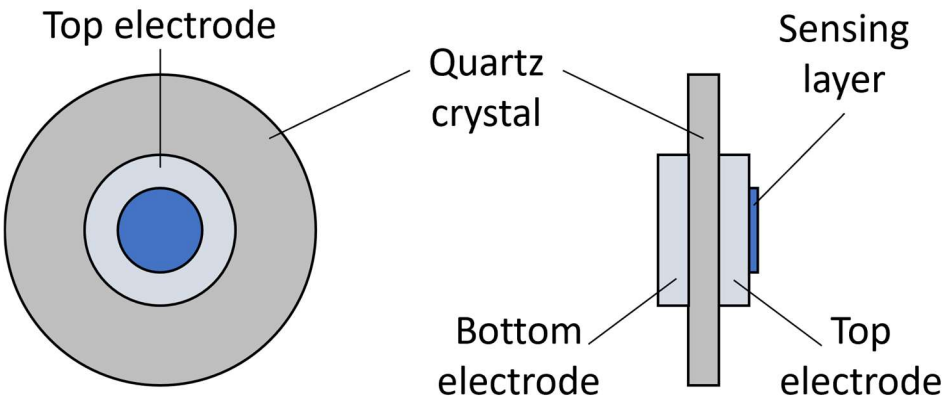

Figure 1. 2 Schematic diagram of a typical QCM sensor (a) top view and (b) side view.

1.2.3 Photoionization detector

The Photoionization detector (PID) uses an ultraviolet light as light source (Figure 1.3). When the target gas absorbs high-energy ultraviolet light, the gas molecules are temporarily excited by ultraviolet light to lose electrons into positively charged ions. The gas ions are detected on the electrodes of the detector, and the gas concentration is calculated according to the potential generated by the electrodes (20, 21). After the detection, the ions quickly combine with the electrons to reconstitute the original gas molecules, so the PID sensor shows a high speed in response and recovery speed (typically 1 second or less). However, the energy of the ultraviolet source limits the type of gas that can be ionized, and the ionization of the impurity gas affects the accuracy of the detection.

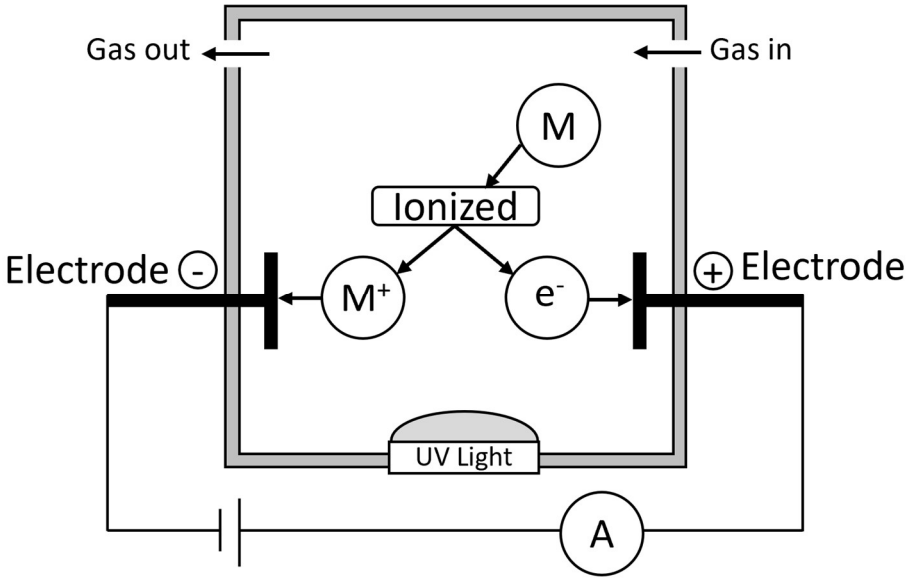

Figure 1. 3 Schematic diagram of a conventional photoionization detector (PID).

1.3 Localized surface plasmon resonance

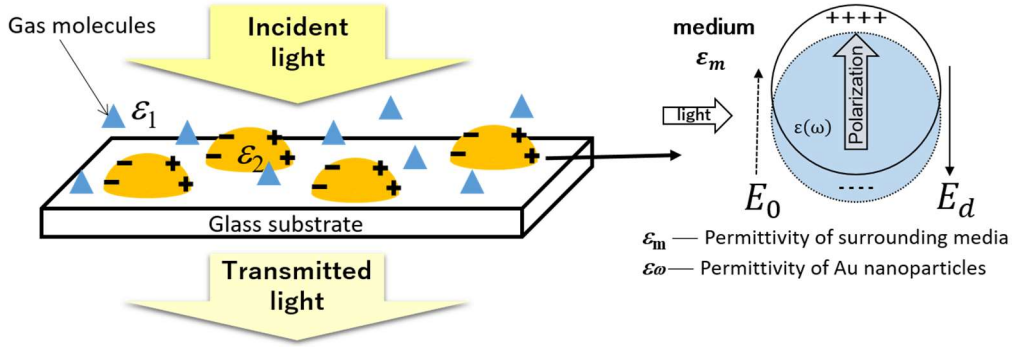

Figure 1. 4 Principle of gas sensing with Au-LSPR gas film

Localized Surface Plasmon Resonance (LSPR) is a phenomenon based on the resonance of electrons on the surface of metal nanoparticles (22, 23). When metal nanoparticles, such as gold or silver, are exposed to light, the free electrons in the metal interact with the electromagnetic field of the incident light. This interaction causes a collective oscillation of the electron cloud on the surface of the nanoparticles relative to their positively charged background. Localized Surface Plasmon Resonance occurs when the frequency of the incident light matches the natural oscillation frequency of the electrons on the surface of the metal nanoparticles. This resonance results in the nanoparticles exhibiting strong light absorption and scattering at specific wavelengths.

The characteristics of LSPR, such as resonance wavelength and intensity, are highly dependent on the size, shape, and material composition of the nanoparticles. Under resonance conditions, the local electromagnetic field near the metal nanoparticles is significantly enhanced. The LSPR properties of metal nanoparticles are extremely sensitive to the permittivity of the surrounding medium. Therefore, when the medium around the nanoparticles changes, the resonance characteristics also change accordingly. This makes LSPR an effective tool for chemical sensing, as it can detect changes in the surrounding environment through shifts in its resonance properties (24, 25). Figure 1.4 shows detecting principle of gas detection using LSPR using a glass substrate with Au nanoparticles on its surface. Polarization $P(\omega)$ can be calculated as follow:

$$P(\omega) = \frac{3}{4\pi} \frac{\varepsilon_m(\varepsilon(\omega) - 1)}{\varepsilon(\omega) + 2\varepsilon_m} E_0$$

Where ε_m is permittivity of surrounding media, $\varepsilon(\omega)$ is dielectric function of NPs, E_0 is external electric field. The resonance appears when $\varepsilon(\omega) = -2\varepsilon_m$, denominator becomes its minimum.

1.4 Method for Detecting the Spatial Distribution of Odor Traces

1.4.1 Gas sensor with mobile robot

Research on obtaining spatiotemporal distribution information in odor plumes using mobile robots equipped with gas sensors has been very popular over the past decade. These odor robots are not only capable of measuring the gradient changes in concentration within odor plumes but can also use concentration differences to localize the source of the odor. This research is particularly notable for its imitation of biological olfaction and can make significant contributions in areas such as disaster relief. Figure 1.5 shows a typical robot equipped with semiconductor sensors (26). This robot detects the start of response and the beginning of recovery by monitoring the relative changes in the output of each gas sensor, enabling it to track and locate plumes. This approach overcomes the inefficiency issues caused by the slow response speed of traditional semiconductor gas sensors.

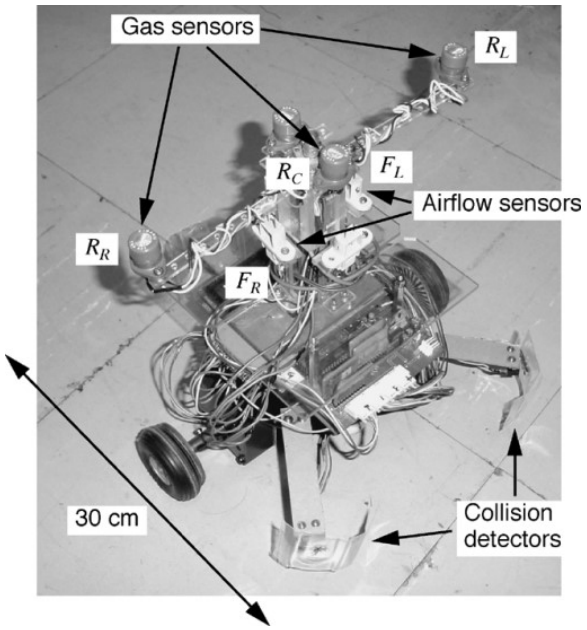

Figure 1. 5 Photograph of mobile robot [26]

1.4.2 Odor visualization

Gas plume visualization with gas sensor array

The concentration distribution of gas plume on a sensor array is visualized as a grayscale image, shown in Figure1.6 (27). Therefore, if the gas sensors respond quickly enough, the direction of gas flow can be obtained from visualizing the movement of the

gas plume. This method not only provides the distribution of gas within a local range but also enables gas monitoring information at specific locations within a larger scale, like a city, by adjusting the distribution of the sensor array. However, due to the limitations of sensor size and their own response times, especially in local ranges, the resolution of the acquired image information is relatively low.

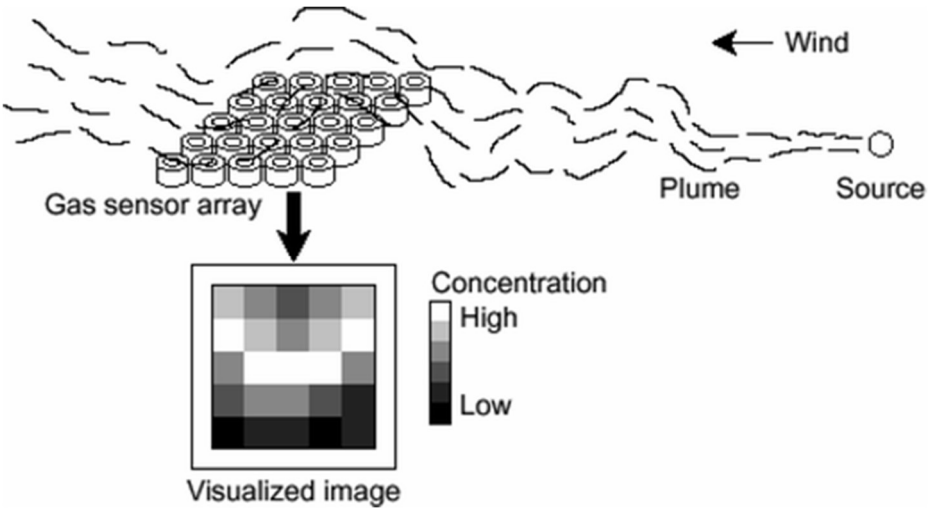

Figure 1. 6 gas flow visualization with gas sensor array [27].

Odor visualization with Enzyme

Enzymes, serving as catalysts in chemical reactions, can facilitate these reactions by lowering the activation energy required (28). Alcohol dehydrogenase (ADH) is an enzyme that catalyzes the oxidation of ethanol, converting it into acetaldehyde (29,30). In this process, ADH assists in transferring hydrogen atoms from ethanol to the coenzyme NAD+. In the reaction mediated by ADH, NAD+ is reduced to NADH. NADH has the characteristic of emitting fluorescence at a specific wavelength, whereas NAD+ does not possess this characteristic (). The concentration of ethanol vapor can be accurately deduced by measuring changes in fluorescence intensity and comparing these with a standard curve of known ethanol concentrations. In reported enzyme-based alcohol sensors, the enzyme is uniformly dispersed on a cotton net. By using a high-sensitivity CCD camera to capture the fluorescence intensity on the cotton net, the spatial distribution of alcohol can be detected (31). This method shows a high sensitivity and selectivity in gas detection.

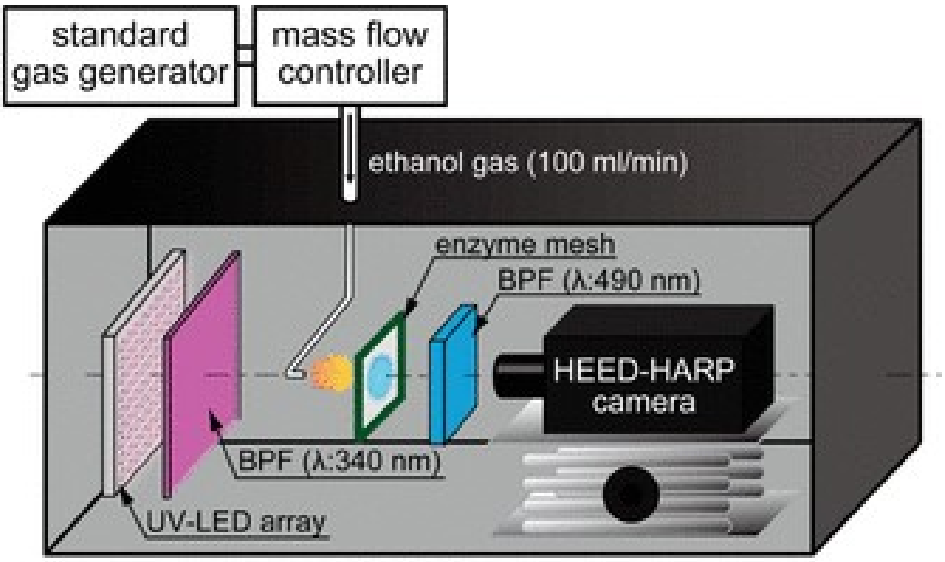

Figure 1. 7 Ethanol vapor visualization measurement system using a biofluorescence method [31].

1.5 Purpose and novelty

Currently, spatiotemporal distribution information of odor traces is primarily acquired through gas sensors located at fixed points or by mobile robots equipped with gas sensors performing one-dimensional scanning. However, the performance of the sensors is a major limitation on the operational speed of the robots during information collection. Additionally, although there have been attempts to visualize the two-dimensional spatial distribution of odor traces using reactions between fluorescent substances and chemicals in odors, the limitations in response time and spatial resolution still limit the realization of real-time visual measurement of odor traces.

The purpose of this research is to develop a gas sensor device based on the plasmon resonance of metal nanoparticles that enables the utilization of spatial distribution information of on-ground odor trace and to establish methods for processing this kind of information.

The research was conducted in 3 steps: 1. Development of high-speed plasmonic gas sensors and mount the sensor on mobile robot for collecting spatial information from on-round odor source; 2. Development of high-speed two-dimensional odor trace visualization system; 3. Collecting real-time distributions of odor traces with visualization system and evaluating its performance.

Novelty:

1. Development of odor robot with one-dimensional LSPR gas sensor for collecting spatial odor Information from on-ground invisible odor sources at a high speed.

2. Development of two-dimensional odor trace visualization system with high spatial resolution.

3. A calibration method has been developed to determine the optimal time while capturing images from on-ground odor traces and reproduce the shape information of odor trace through visualized images.

1.6 Thesis organization

The organization of this research is as follow:

Chapter 1 introduces the background of the study. It includes the significance of odor information, sensors and methods for detecting odor information, and research on the visualization of odor traces. Finally, the research objective: to acquire spatiotemporal distribution information of odor information.

Chapter 2 proposed an odor robot for collecting spatial distribution of on-ground odor traces with high speed LSPR sensor module.

Chapter 3 describes the design and fabrication of a two-dimensional odor trace visualization system by combining an LSPR substrate with a CCD camera. It validates the feasibility of LSPR imaging through differential image analysis of gas flow images obtained by transmission type and odor trace images obtained by reflection type.

Chapter 4 tested the performance of two-dimensional odor trace imaging system for on-ground odor trace acquisition. The angle of the camera was adjusted in the two-dimensional trace visualization system to obtain visualization images based on scattered light, avoiding the impact of the camera body leaving traces in the reflective images on the final imaging results. At the same time, through control experiments, it verifies the imaging effects of the LSPR substrate relative to non-LSPR substrates and establishes a method for determining the best time to capture images that can reflect the shape of the odor traces.

Chapter 5 summarizes the content of chapters 2, 3, and 4 and provides an outlook for future work.

Reference

(1) Firestein, S. How the olfactory system makes sense of scents. Nature 2001, 413, 211–218. https://doi.org/10.1038/35093026.
(2) Murlis, J.; Elkinton, J.S.; Carde, R.T. Odor Plumes and How Insects Use Them. Annu. Rev. Entomol. 1992, 37, 505–532. https://doi.org/10.1146/annurev.en.37.010192.002445.
(3) Xu, H. X.; Kitai, K.; Minami, K.; Nakatsu, M.; Yoshikawa, G.; Tsuda, K.; Shiba, K.; Tamura, R. Determination of quasi-primary odors by endpoint detection. Scientific Reports 2021, 11 (1). DOI: 10.1038/s41598-021-91210-6.
(4) Kuroda, S.; Nakaya-Kishi, Y.; Tatematsu, K.; Hinuma, S. Human Olfactory Receptor Sensor for Odor Reconstitution. Sensors 2023, 23 (13). DOI: 10.3390/s23136164.
(5) Saasa, V.; Malwela, T.; Beukes, M.; Mokgotho, M.; Liu, C. P.; Mwakikunga, B. Sensing Technologies for Detection of Acetone in Human Breath for Diabetes Diagnosis and Monitoring. Diagnostics 2018, 8 (1). DOI: 10.3390/diagnostics8010012.
(6) Carmichael, G. R.; Ferm, M.; Thongboonchoo, N.; Woo, J. H.; Chan, L. Y.; Murano, K.; Viet, P. H.; Mossberg, C.; Bala, R.; Boonjawat, J.; et al. Measurements of sulfur dioxide, ozone and ammonia concentrations in Asia, Africa, and South America using passive samplers. Atmospheric Environment 2003, 37 (9-10), 1293-1308. DOI: 10.1016/s1352-2310(02)01009-9.
(7) Zimmerfaust, R. K.; Finelli, C. M.; Pentcheff, N. D.; Wethey, D. S. ODOR PLUMES AND ANIMAL NAVIGATION IN TURBULENT WATER-FLOW - A FIELD-STUDY. Biological Bulletin 1995, 188 (2), 111-116. DOI: 10.2307/1542075.
(8) Li, C. Y.; Hou, J.; Cheng, W. Y.; Gai, W. M. A multiagent-based modeling approach for emergency evacuation plan optimization during toxic gas releases within chemical plants. Process Safety and Environmental Protection 2022, 163, 543-557. DOI: 10.1016/j.psep.2022.05.026.
(9) Malik, R. Does Archaeology Stink? Detecting Smell in the Past Using Headspace Sampling Techniques. International Journal of Historical Archaeology 2021, 25 (2), 273-296. DOI: 10.1007/s10761-020-00552-w.
(10) Baron, R.; Saffell, J. Amperometric Gas Sensors as a Low Cost Emerging Technology Platform for Air Quality Monitoring Applications: A Review. ACS Sens. 2017, 2, 1553–1566. https://doi.org/10.1021/acssensors.7b00620.
(11)Tai, H.L.; Duan, Z.H.; Wang, Y.; Wang, S.; Jiang, Y.D. Paper-Based Sensors for Gas, Humidity, and Strain Detections: A Review. ACS Appl. Mater. Interfaces 2020, 12, 31037–31053. https://doi.org/10.1021/acsami.0c06435.

(12) Wang, Z.; Zhu, L.; Liu, J.W.; Wang, J.N.; Yan, W. Gas Sensing Technology for the Detection and Early Warning of Battery Thermal Runaway: A Review. Energy Fuels 2022, 36, 6038–6057. https://doi.org/10.1021/acs.energyfuels.2c011216038.
(13) He, T.Y.Y.; Wen, F.; Yang, Y.Q.; Le, X.H.; Liu, W.X.; Lee, C.K. Emerging Wearable Chemical Sensors Enabling Advanced Inte-grated Systems toward Personalized and Preventive Medicine. Anal. Chem. 2023, 95, 490–514. https://doi.org/10.1021/acs.analchem.2c04527.
(14) Lin, T. T.; Lv, X.; Li, S.; Wang, Q. J. The Morphologies of the Semiconductor Oxides and Their Gas-Sensing Properties. Sensors 2017, 17 (12). DOI: 10.3390/s17122779.
(15) Raju, P.; Li, Q. L. Review-Semiconductor Materials and Devices for Gas Sensors. Journal of the Electrochemical Society 2022, 169 (5). DOI: 10.1149/1945-7111/ac6e0a.
(16) Nikolic, M. V.; Milovanovic, V.; Vasiljevic, Z. Z.; Stamenkovic, Z. Semiconductor Gas Sensors: Materials, Technology, Design, and Application. Sensors 2020, 20 (22). DOI: 10.3390/s20226694.
(17) Songkhla, S. N.; Nakamoto, T. Overview of Quartz Crystal Microbalance Behavior Analysis and Measurement. Chemosensors 2021, 9 (12). DOI: 10.3390/chemosensors9120350.
(18) Kikuchi, M.; Tsuru, N.; Shiratori, S. Recognition of terpenes using molecular imprinted polymer coated quartz crystal microbalance in air phase. Science and Technology of Advanced Materials 2006, 7 (2), 156-161. DOI: 10.1016/j.stam.2005.12.004.
(19) Dehari, Y.; Takei, Y.; Koyama, S.; Nanto, H.; Seki, S. QCM Gas Sensor with Organic Nanowire Film as Molecular Recognition Membrane. Sensors and Materials 2010, 22 (4), 175-181.
(20) Sun, J. H.; Guan, F. Y.; Cui, D. F.; Chen, X.; Zhang, L. L.; Chen, J. An improved photoionization detector with a micro gas chromatography column for portable rapid gas chromatography system. Sensors and Actuators B-Chemical 2013, 188, 513-518. DOI: 10.1016/j.snb.2013.07.066.
(21) Poole, C. F. Ionization-based detectors for gas chromatography. Journal of Chromatography A 2015, 1421, 137-153. DOI: 10.1016/j.chroma.2015.02.061.
(22) Willets, K. A.; Van Duyne, R. P. Localized surface plasmon resonance spectroscopy and sensing. Annual Review of Physical Chemistry 2007, 58, 267-297. DOI: 10.1146/annurev.physchem.58.032806.104607.

(23) Cao, J.; Sun, T.; Grattan, K. T. V. Gold nanorod-based localized surface plasmon resonance biosensors: A review. Sensors and Actuators B-Chemical 2014, 195, 332-351. DOI: 10.1016/j.snb.2014.01.056.
(24) Sepúlveda, B.; Angelomé, P. C.; Lechuga, L. M.; Liz-Marzán, L. M. LSPR-based nanobiosensors. Nano Today 2009, 4 (3), 244-251. DOI: 10.1016/j.nantod.2009.04.001.
(25) Zhao, J.; Zhang, X. Y.; Yonzon, C. R.; Haes, A. J.; Van Duyne, R. P. Localized surface plasmon resonance biosensors. Nanomedicine 2006, 1 (2), 219-228. DOI: 10.2217/17435889.1.2.219.
(26) Ishida, H.; Nakayama, G.; Nakamoto, T.; Moriizumi, T., Controlling a gas/odor plume-tracking robot based on transient responses of gas sensors. IEEE Sens. J. 2005, 5 (3), 537-545.
(27) Ishida, H.; Yamanaka, T.; Kushida, N.; Nakamoto, T.; Moriizumi, T. Study of real-time visualization of gas/odor flow image using gas sensor array. Sensors and Actuators B-Chemical 2000, 65 (1-3), 14-16. DOI: 10.1016/s0925-4005(99)00415-3.
(28) Garcia-Viloca, M.; Gao, J.; Karplus, M.; Truhlar, D. G. How enzymes work: Analysis by modern rate theory and computer simulations. Science 2004, 303 (5655), 186-195. DOI: 10.1126/science.1088172.
(29) Williams, A. K.; Hupp, J. T. Sol-gel-encapsulated alcohol dehydrogenase as a versatile, environmentally stabilized sensor for alcohols and aldehydes. Journal of the American Chemical Society 1998, 120 (18), 4366-4371. DOI: 10.1021/ja973772c.
(30) Crabb, D. W.; Matsumoto, M.; Chang, D.; You, M. Overview of the role of alcohol dehydrogenase and aldehyde dehydrogenase and their variants in the genesis of alcohol-related pathology. Proceedings of the Nutrition Society 2004, 63 (1), 49-63. DOI: 10.1079/pns2003327.
(31) Arakawa, T.; Sato, T.; Iitani, K.; Toma, K.; Mitsubayashi, K. Fluorometric Biosniffer Camera "Sniff-Cam" for Direct Imaging of Gaseous Ethanol in Breath and Transdermal Vapor. Analytical Chemistry 2017, 89 (8), 4495-4501. DOI: 10.1021/acs.analchem.6b04676.

Chapter 2 Collecting spatial odor information from on-ground odor sources using an odor robot with high-speed LSPR gas sensor module

2.1 Introduction

As introduced in Chapter 1, using mobile robots equipped with gas sensors to actively scan and acquire spatial distribution information of odor traces is an effective method. Over the past two decades, there has been a significant achievement on research aimed at emulating biological olfactory tracking mechanisms (1-2) through the use of mobile robots equipped with artificial olfactory systems for the proactive localization of gas sources (3-7). In contrast to passive gas-sensing systems, this active sensing approach is capable of odor detection, tracking, and source localization. In early work, many groups reported that odor robot can track a gas plume in the air and find odor sources using a semiconductor gas sensor and search algorithms. (8-11) In mapping the gas distribution, the spatial resolution is determined by combining the sensor response speed and speed of motion of the gas plume (12-14). A variety of methodologies have been employed to enhance the efficacy of odor-detecting robots, including the deployment of a multi-robot olfactory system (15-18), the implementation of bioinspired robotic designs (19-21), and the integration of different sensor types (22-24). Some of the research focused on the improvement of tracing algorithm (25-32). Most of these robots were designed for odor source localization. The response speed of commercially available semiconductor gas sensor based on a chemical reaction, which is commonly used for these robot systems, is not high (typically longer than 10 s). The response speed of the sensor is a major limit to improving the operating speed and promoting the application of a gas-sensing robot for collecting spatial distribution from odor source.

The application of localized surface plasmon resonance (LSPR) in gas sensing presents a promising approach for the development of high-speed gas sensors for mobile robots (33-35). LSPR occurs when the frequency of incident light matches the frequency of the electromagnetic resonance of the noble-metal nanoparticle, and it causes strong light absorption and scattering (36). Light absorption due to LSPR is a physical phenomenon that changes with the permittivity of the surrounding medium, such as gas environment, and it responds quickly to gas exposure. This phenomenon is used in chemical sensors and biosensors by applying optical methods. (37,38) Methods have

already been developed to enhance the property of LSPR for biosensing. These include the integration of an optical waveguide system (39), the employment of specialized substrate surfaces (40), and the incorporation of hollow structural designs (41).

Chen et.al has developed a simple method of fabricating an LSPR gas-sensor substrate by depositing Au nanoislands on a glass substrate (42). The fabrication process involves multiple cycles of Au sputtering followed by annealing at high temperatures, a procedure essential for the control of nanostructure of the Au nanoparticles. The accurate control of the size and particle density of Au nanoparticles proved to be effective in increasing the sensitivity of the sensor (43). Furthermore, molecular selectivity can be enhanced to the sensor through the application of a molecularly imprinted polymer coating on the LSPR substrate (44).

This chapter present the development of an Au-LSPR-based high-speed gas sensor module. This module was integrated onto a crawler robot, resulting in a robot system capable of gathering data from on-ground odor sources with high spatial resolution. Distinct from other odor sensing robots, the detection target of this system is not atmospheric gas plumes, but invisible on-ground odor sources. These include footprints, artificial odor markers, or other residual traces on surfaces that carry information about past events. To demonstrate the capabilities of the robot, it successfully read spatial odor information from an arrayed odor source on the ground similar to the reading of a barcode and encoded byte data via the distribution of evaporated gas from odor sources.

2.2 Experimental

2.2.1 Concept of the On-Ground Odor Information Collecting Robot

The concept of an on-ground odor information collecting robot is shown in Figure 2.1. The target analytes of the proposed robot are gases that have evaporated from invisible odor sources on the ground, such as a footprint, adhered substances, spilled liquid or artificial odor marker. For the acquisition of high spatial resolution data regarding the distribution of these odor sources, the robot is equipped with fine tubing dedicated to gas sampling. This tubing is strategically positioned close to the ground to optimize the detection process. The gas from the odor source is suctioned into the LSPR gas sensor module by a vacuum pump. After detection, the gas is exhausted to the opposite side of the robot system to avoid contaminating the sampling spot.

Figure 2.2 shows the developed odor robot with an LSPR sensor module. The LSPR gas sensor module is positioned in front of the shield of a crawler robot (Zumo Robot for Arduino, POLOLU, USA). Software was wirelessly uploaded to a microcontroller

(Arduino YUN, Arduino LLC, USA) to control the robot and obtain output signals from the sensor. The distance from the stainless-steel sampling tubing to the ground is about 1 mm to ensure that the target gas reaches sensors quickly without polluting the tubing.

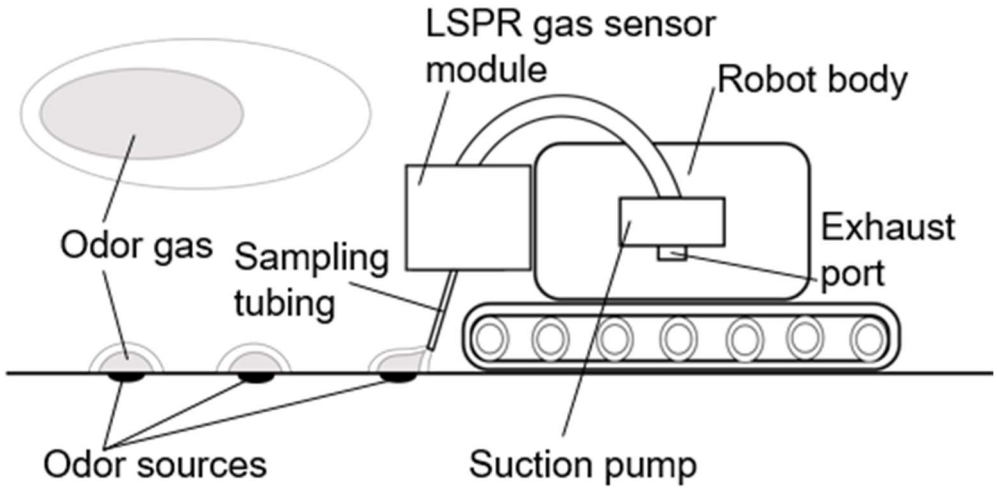

Figure 2. 1 Concept of collecting spatial odor information from an on-ground odor source.

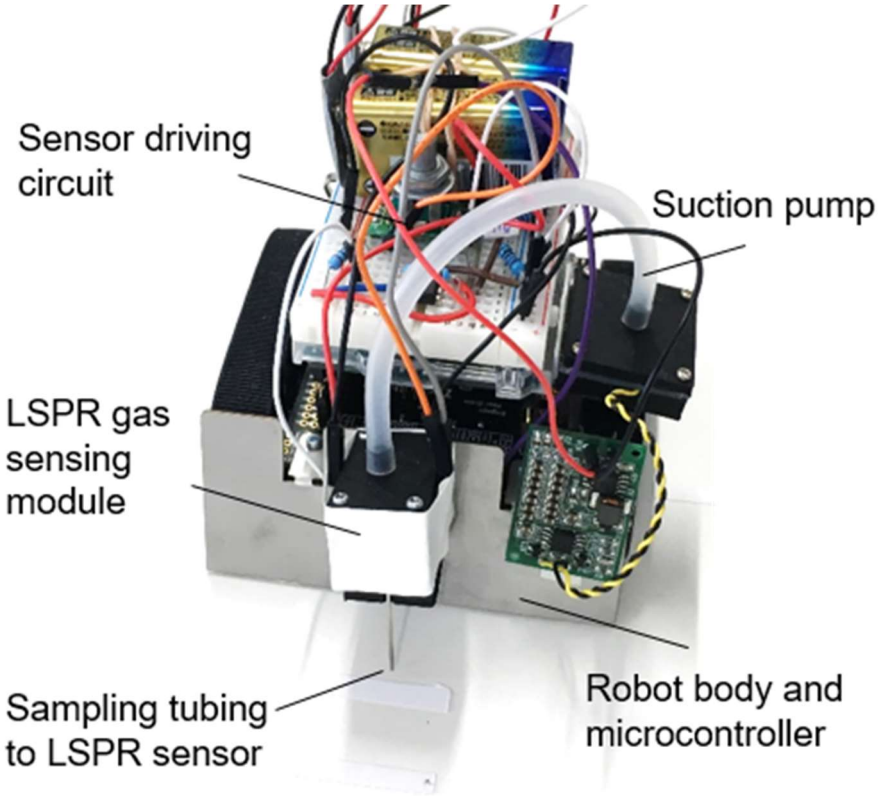

Figure 2. 2 Photograph of a mobile robot with the LSPR gas sensing module.

2.2.2 Fabrication of the LSPR gas-sensitive substrate.

A gas-sensitive Au nano-island structure was formed on a glass substrate with a size of 26 mm × 1.0 mm × 0.9 mm (S1126, Matsunami, Japan) as follows. The glass substrate underwent a sequential cleaning process with purified water, acetone and ethanol. After the drying process with a stream of nitrogen gas, the glass substrate was subjected to a 5-minute argon gas plasma treatment using a plasma cleaner (Harrick, PDC-001K). The cleaned glass substrate was immersed in a 1:15 3-aminopropyltriethoxysilane (APTES) (LS-3150, Shin-Etsu Chemical, Japan) ethanol solution for 24 hours at room temperature to immobilize Au nanoparticles more strongly on the surface of glass substrate. Ultrasonication was then conducted in ethanol for 10 minutes to remove excess APTES molecules physically attached to the glass surface. Au nanoparticles were deposited on the APTES-treated substrate by sputtering (20 mA, 6 s) using a sputtering machine (SC-701HMC II, Sanyo Denshi, Japan). The deposited Au particles are corresponding to a 3 nm layer under this setting in amount. After sputtering deposition, the substrate is subjected to a heat treatment at 200°C for 1 hour, facilitating the agglomeration process to form the nano-island structure. To further enhance the density of the Au nano-islands on the substrate, the sputtering and heat treatment procedure was repeated. The LSPR substrates that were deposited once, twice, and thrice are referred to as 3-nm, 6-nm, and 9-nm LSPR substrates, respectively.

2.2.3 Fabrication of the gas-sensing module.

The gas sensor module comprised a gas chamber fabricated using a three-dimensional printer (Printrbot Play, Printerbot, USA) and a polylactic-acid-based thermoplastic (PolyMax PLA, Polymaker, China), light-emitting diode (LED) light source (MVR5373X, Stanley Electric, Japan), photodiode (S9648-100, Hamamatsu, Japan), Au LSPR substrate, and suction pump (modified from a YS-AIR-SMD01, YS Design Studio, Japan). Figure 2.3 shows the design of the sensor module body, with an overall size of 30 mm × 60 mm × 42 mm. Two pockets (with dimensions of 1.2 mm × 26.5 mm × 10.5 mm in each) in the sensor module body held two pieces of LSPR substrate. The gas-sensitive surfaces of the substrates were oriented to face inward, separated by a partition plate featuring a through-hole with a diameter of 5.0 mm. A small gas chamber was formed by the hole and the substrates, with the top and bottom sides of the chamber being connected to a gas inlet and outlet, respectively. Cylindrical holes were present on the left and right sides of the module to accommodate the LED light source and photodiode, respectively. The optical system (LSPR substrate, light source, photodiode) functioned as a transmittance detector. The lid of the module was sealed with a silicone

gasket and secured using four screws The LED light source's wavelength peak was 630 nm, which covered the maximum variation range of the LSPR substrates when exposed to air and ethanol environment. The gas pathway's total volume in the module, extending from the sampling tubing to the outlet, was 240 µL. Concurrently, the suction flow rate of the pump connected to the assembled module approximated 1700 µL/s. For this design, the time required for gas exchange in the chamber, a factor influencing signal delay, was estimated to be around 0.15 s. The signal obtained from the photodiode was amplified 20 times with an instrumentation amplifier (AD620, Analog Devices, USA) and input to an analog input port of the Arduino microcontroller.

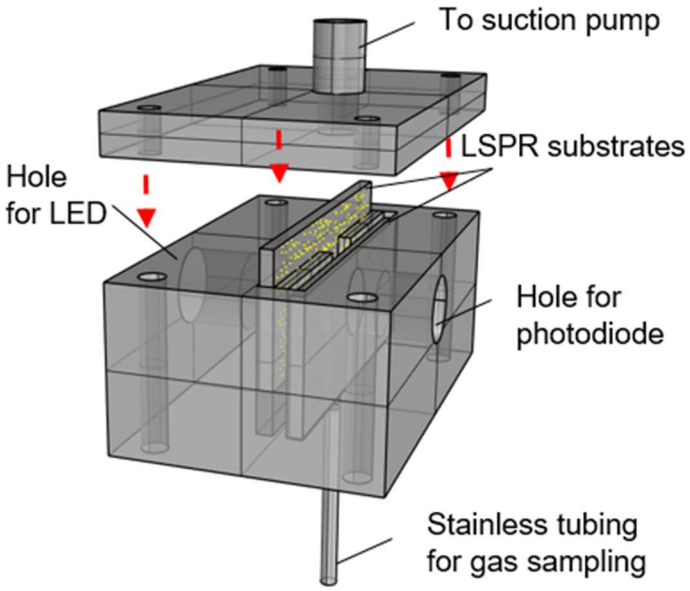

Figure 2. 3 LSPR gas-sensing module fabricated using a three-dimensional printer. Openings on left and right sides were used for an LED light source and photodiode to detect the change in intensity of light passing through the LSPR substrate when the gas environment changed. A suction pump was connected to the top of the module to create a gas flow path between two LSPR substrates.

2.3 Result and discussion

2.3.1 Characterization of the Au-NP film and LSPR gas-sensing module.

Figure 2.4A shows the photographs of the 3-, 6- and 9-nm (with SEM image) LSPR substrates for different sputtering conditions. Transmittance spectra of the fabricated LSPR substrates were measured by a spectrophotometer (UV-1800, Shimadzu, Japan) and results are presented in Figure 2.4B. Solid and dashed lines respectively show the transmittance spectra of the LSPR substrates when exposed to air and ethanol. A decrease in transmittance was observed when the LSPR substrate was exposed to ethanol from air.

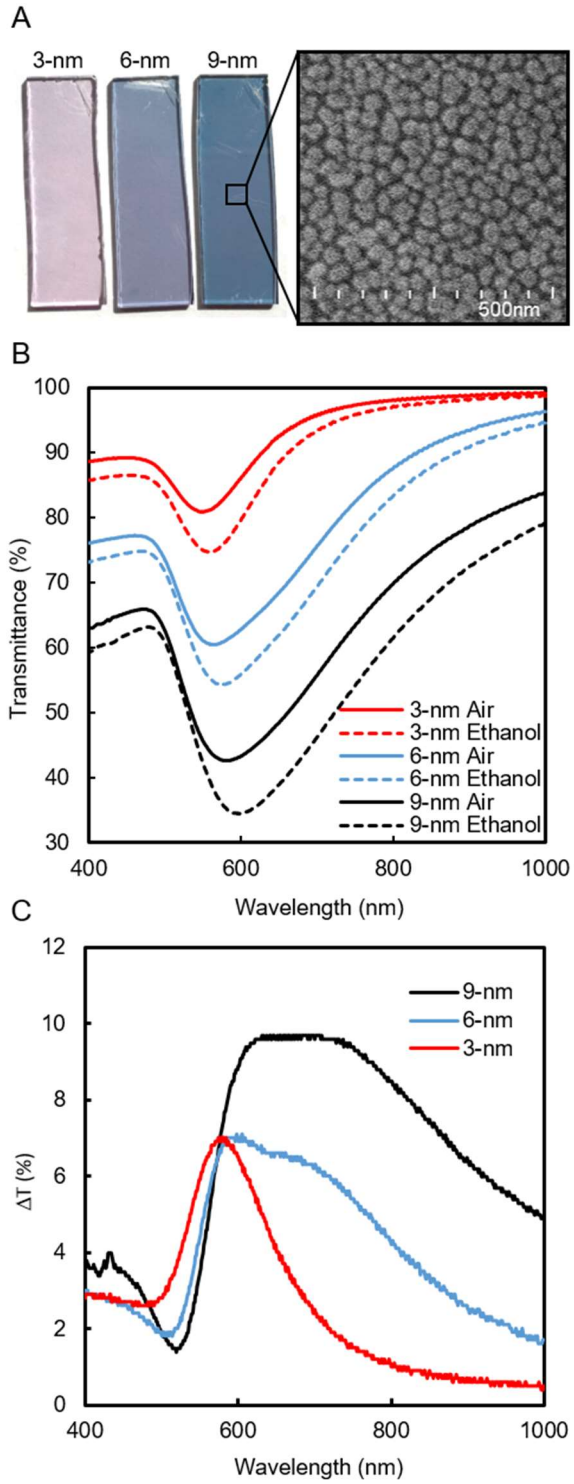

Figure 2. 4 Characteristics of the fabricated LSPR gas-sensitive substrate. (A) Photographs of glass substrates sputtered with one, two, and three Au nanoparticle layers, respectively referred to as 3-, 6-, and 9 nm layers. SEM image shows the nano-island structure of 9 nm LSPR substrate. (B) Transmittance spectrum of the LSPR substrate. Solid lines represent the transmittance spectrum when the substrate was exposed to air; dotted lines represent the transmittance spectrum when the substrate was exposed to saturated ethanol gas. (C) Transmittance variation of the LSPR substrate when exposed to air and saturated ethanol gas.

Figure 2.4C shows the transmittance change of the three substrates for different sputtering conditions at wavelengths from 400 to 1000 nm. For the 3- and 6-nm substrates, the peak of transmittance variation was observed around 580 nm, exhibiting an amplitude of 7%. In contrast, the peak for the 9-nm substrate was observed in the range of 620 to 730 nm, with a larger amplitude of 9%.

The total transmittance change T_{total}, defined as the sum of difference of T_{air} (λ) and $T_{ethanol}$ (λ), at each wavelength in the range of 400 to 760 nm was used as an evaluation according to the following formula.

$$\boldsymbol{T_{total}} = \sum_{400}^{760} |\boldsymbol{T_{air}}(\lambda) - \boldsymbol{T_{ethanol}}(\lambda)| \cdot \Delta\lambda \quad \cdots\cdots (1)$$

T_{total} was greatest for the 9-nm LSPR substrate (2288.8), followed by the 6-nm substrate (1704.0) and 3-nm substrate (1352.1). This result shows that the re-sputtering and re-annealing method improves the sensitivity of the Au LSPR substrate under the tested conditions. According to increasing of density and size of the Au islands by the process cycle, absorption cross section which contribute to the absorption change of the substrate and LSPR peak shift are occurred.[43]

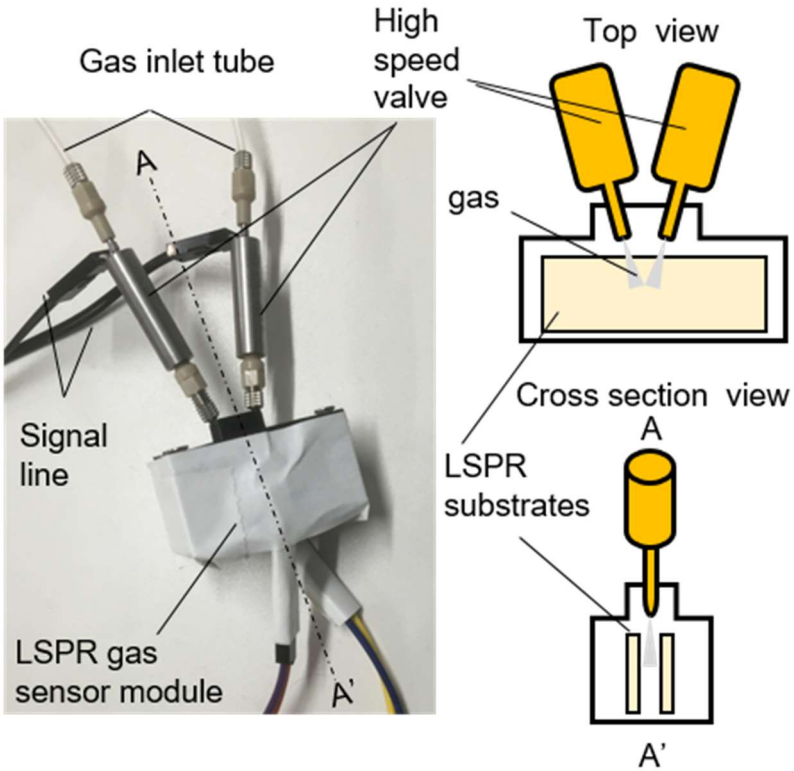

Figure 2. 5 Design of a high-speed gas exchange system for module evaluation. Two high-speed valves were connected to the gas-sensing module, with one open and the other closed to create a gas switching environment. The openings in the cover had a 30° angle that ensured that the ejected gas aligned with the center of the chamber.

The sensor module was connected to two high-speed gas valves with another cover to evaluate the response speed of the LSPR substrate, as shown in Figure 2.5. Nozzles were placed close to the LSPR substrate to ensure that gas or air between two sensor substrates can be exchanged rapidly. The time courses of gas response were shown in Figure 2.6 (inset), with top and bottom signals respectively corresponding to sensors exposed to air and ethanol. The high-speed valves were switched every 0.2 to 0.02 s such that one was open and the other was closed, which means the sensor module tracked the gas switching frequency of the high-speed valves from 2.5 to 25 Hz. Figure 2.6 shows the relationship between the change in the sensor signal and the frequency of gas exchange.

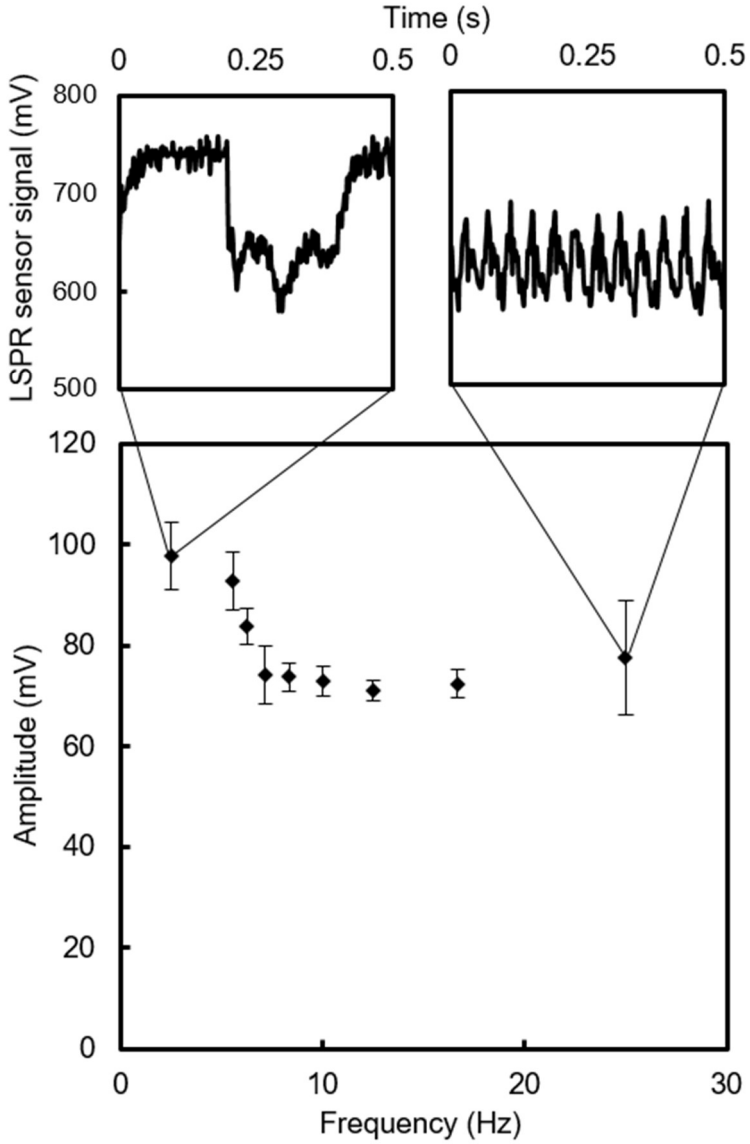

Figure 2. 6 Frequency response of the module. The gas exchange frequency was set to 2.5, 5.56, 6.25, 7.14, 8.33, 10, 12.5, 16.67, and 25 Hz. Insets show time courses of the sensor output signal at 2.5 and 25 Hz.

With an increase in the gas switching speed, the output signal of the sensor only shows a decrease from 97.81 to 71.05 mV when exchanged from air to ethanol. This indicates the sensor's effective performance in rapidly changing gas environments. The waveform of the signal changed from a rectangular wave to a triangle wave, which explains drops at 5.56 and 6.25 Hz. When the frequency increased to 25 Hz, the peaks sharpened, and it was hardly possible to take the average with a sample size of 500 every second. This may contribute to the unpredicted increase in the signal variation at 25 Hz. The dependency of the sensor signal on ethanol gas concentration was also tested. The gas sampling tubing of the LSPR sensor module was connected to an airbag containing ethanol gas at concentrations of 5000, 10,000, 15,000, and 20,000 ppm. The results are shown in Figure 2.7.

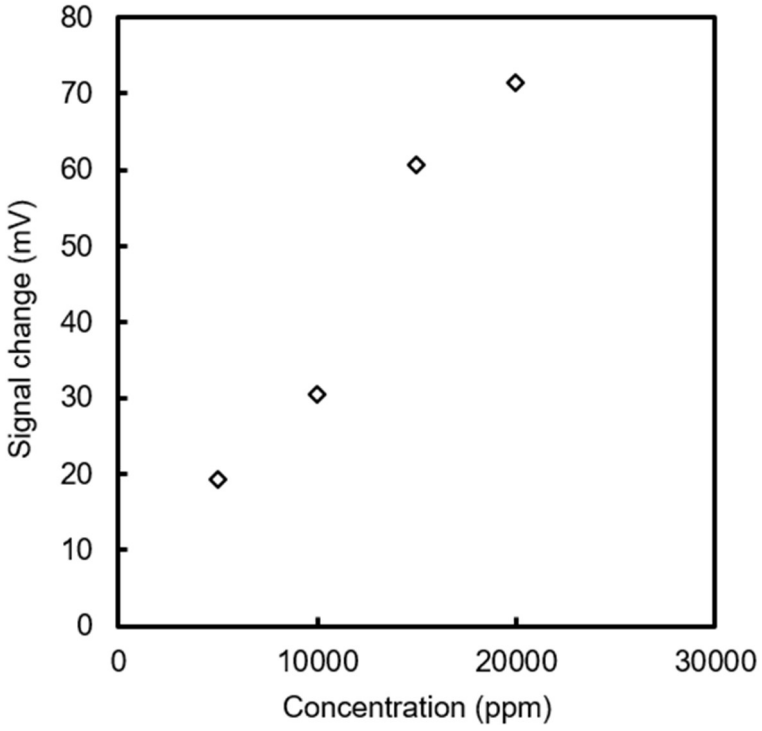

Figure 2. 7 Ethanol gas calibration plot for the LSPR gas-sensing module.

The change in the sensor signal from the signal measured for clean air has a proportional relationship with the gas concentration that is consistent with the theoretical model (45). Lower limit of sensing range of the module is approximately 4,300 ppm which calculated from signal noise ratio (S/N =1) with 20,000 ppm of ethanol gas. Figure S.1 shows the sensing performance of LSPR gas sensor module. Average response time and recovery time were 21.75 ms and 60.25 ms respectively (n=4). The evaluation of the sensor signal's repeatability was based on a series of gas pulse measurements. The relative standard deviations for the sensor signal with air and ethanol gas were found to be similar, approximately 0.34%.

2.3.2 On-ground odor source detection with the robot.

A series of basic experiments for on-ground gas source detection were conducted using a robot equipped with the developed LSPR gas-sensing module. All experiments with the robot were conducted on a clean flat table coated with melamine resin, in a windless room at room temperature.

Figure 2.8A shows the experimental set up. Initially, we measured the sensor signal from the odor source placed at varying intervals, as indicated in course A. Eleven pieces of paper, each with a length of 50 mm and a width of 5 mm, were stuck to the experiment table at specific intervals. These intervals were set at 2.5, 2.5, 2.5, 4.5, 4.5, 4.5, 8.5, 8.5, and 16.5 cm, representing artificial markers for the odor or gas source. The start position of the robot was set 15 cm from the first odor source. Out of the eleven pieces, the final eight were wet with ethanol solution and served as the odor sources. Meanwhile, the first piece of paper was utilized as a marker of the starting position. The robot passed these odor sources at a speed of 10 cm/s. The sensor signal obtained during the experiment is shown in Figure 2.8B. Ten peaks appear at about 5.11, 20.98, 29.99, 38.57, 43.31, 47.53, 51.77, 54.96, 57.32 and 59.96 cm. The differences between the measured values and actual distances are within 0.31 cm, which means the LSPR gas sensor module accurately reflects the positions of the gas sources to a certain degree of precision. Furthermore, the LSPR gas-sensing module responded quickly when the robot approached the gas sources and recovered quickly when the robot moved away from the gas sources. The time delay calculated from the results is 0.031 s. However, when the robot passed the first four gas sources, the sensor signal did not fully recover to the value corresponding to air. This suggests that at this travel speed, a distance of 2.5 cm is close to the spatial resolution of the robot system. Discriminating between odor sources can be challenging when the valley between signal peaks rises or is shifted by noise.

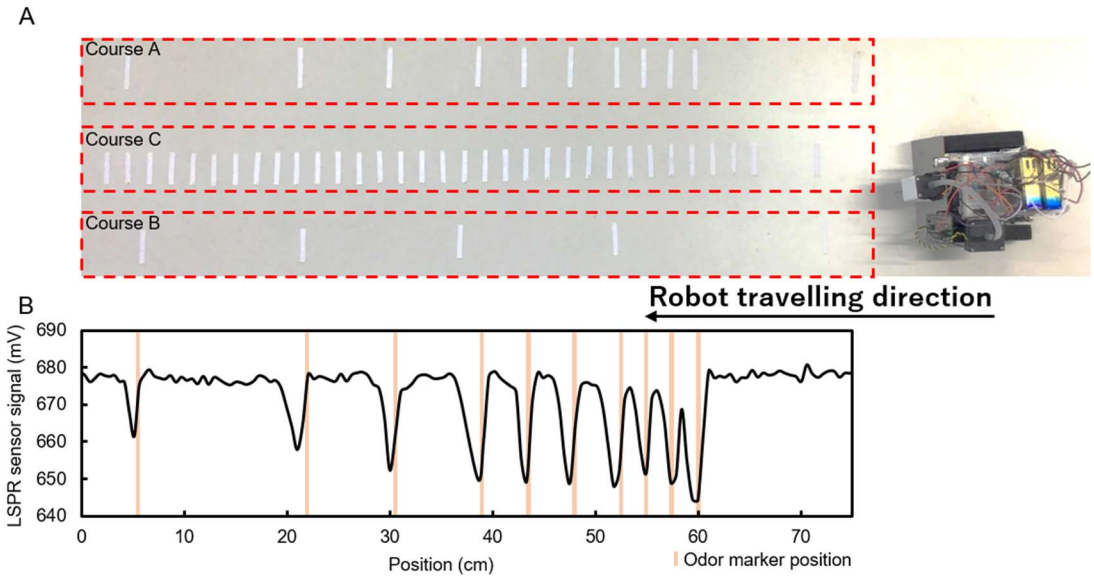

Figure 2. 8 Robot courses of on-ground odor sources. (A) Photographs of robot courses with different arrangements of odor sources. Course A: intervals of ethanol gas sources were set to 2.5, 2.5, 2.5, 4.5, 4.5, 4.5, 8.5, 8.5, and 16.5 cm. Course B: 20 cm interval after the start point and 15 cm intervals between other points. Course C: 6 cm intervals after the start point and before the end point, 2 cm intervals between other points. (B) Sensor response when the robot passed through gas sources of course A.

To clarify the spatial resolution of on-ground odor source detection, a 50% valley method was used as a criterion for discriminating two odor sources from signal peaks. This ratio is that of the peak signal value and valley signal value between peaks. The ratio can be calculated from a single peak. According to this method, the spatial resolution of the robot system was about 2.5 cm when moving past ethanol markers at 10 cm/s. In addition, we measured gas signals from the same odor marker 60 s after the first measurement in the same manner. The peak signal decreased to 41% of the first measurement (data not shown). This may due to the effect of ethanol evaporating from the floor material (i.e., paper) and shows that ethanol can be used as rewritable, invisible and biosafe odor marker; e.g., a multi robot system with pheromone marker communication can be used in an office or hospital. In the following experiments, the preparation of the ethanol marker is performed immediately before the robot is used to avoid the evaporation effect.

To further investigate the performance of the robot with LSPR sensing module, the signal changes when robot passed gas sources at different speeds were obtained. Four gas sources were set using the same method as described earlier, with intervals of 15 cm, starting from a point 20 cm away from the first source (course B). The robot passed these odor sources at speeds of 6.33, 11, 15.7, 20.3, 25, 29.7 and 34.3 cm/s. The results are shown in Figure 2.9A. The peak positions shifted backward from the starting point

gradually owing to the sensor delay with gas exchanging in the chamber (taking around 0.15 s) mentioned above. The relationship between the shift and robot travel speed was thus linear. Figure 2.9B shows the relation between robot travel speed and position shift. As the robot's speed increased, the average positional shift in four runs rising from 0.43 cm to 5.38 cm. The negative extrapolated value of the position shift at zero speed indicates the width of a paper odor marker of 5 mm. Figure 2.9C shows the spatial resolution calculated from the same data for different travel speeds. As the robot's speed increases from 6.33 to 34.3 cm/s, the spatial resolution becomes worse, from 3.2 to 7.77 cm. The spatial sampling rate, which is connected to the spatial resolution, was determined by the fixed temporal sampling rate and travel speed of the system. However, the spatial resolution of around 3.2 cm seems to be a lower limit on the plotted curve. The limit may be due to the diffusion layer of ethanol gas for the marker dimensions used and the atmospheric conditions in the room.

Also, we used different concentration of ethanol diluted with glycerin (80%, 60%, 45%, 28%) as gas sources to verify the relationship between the signal change value and target concentration. The result was shown in Figure 2.9D. The response values were (relative values to 100% ethanol), 62.61%, 46.73%, 30.88%, 18.80%, respectively. The signal changes are deceased lineally with decreasing of ethanol concentration. Furthermore, acetone and hexane were also used as gas sources, and the signal change values were recorded as relative values to 100% ethanol. The response value of acetone and hexane were 93.89% and 58.35%, 5 times average, which means the sensor robot can response to different kind of volatile organic compounds.

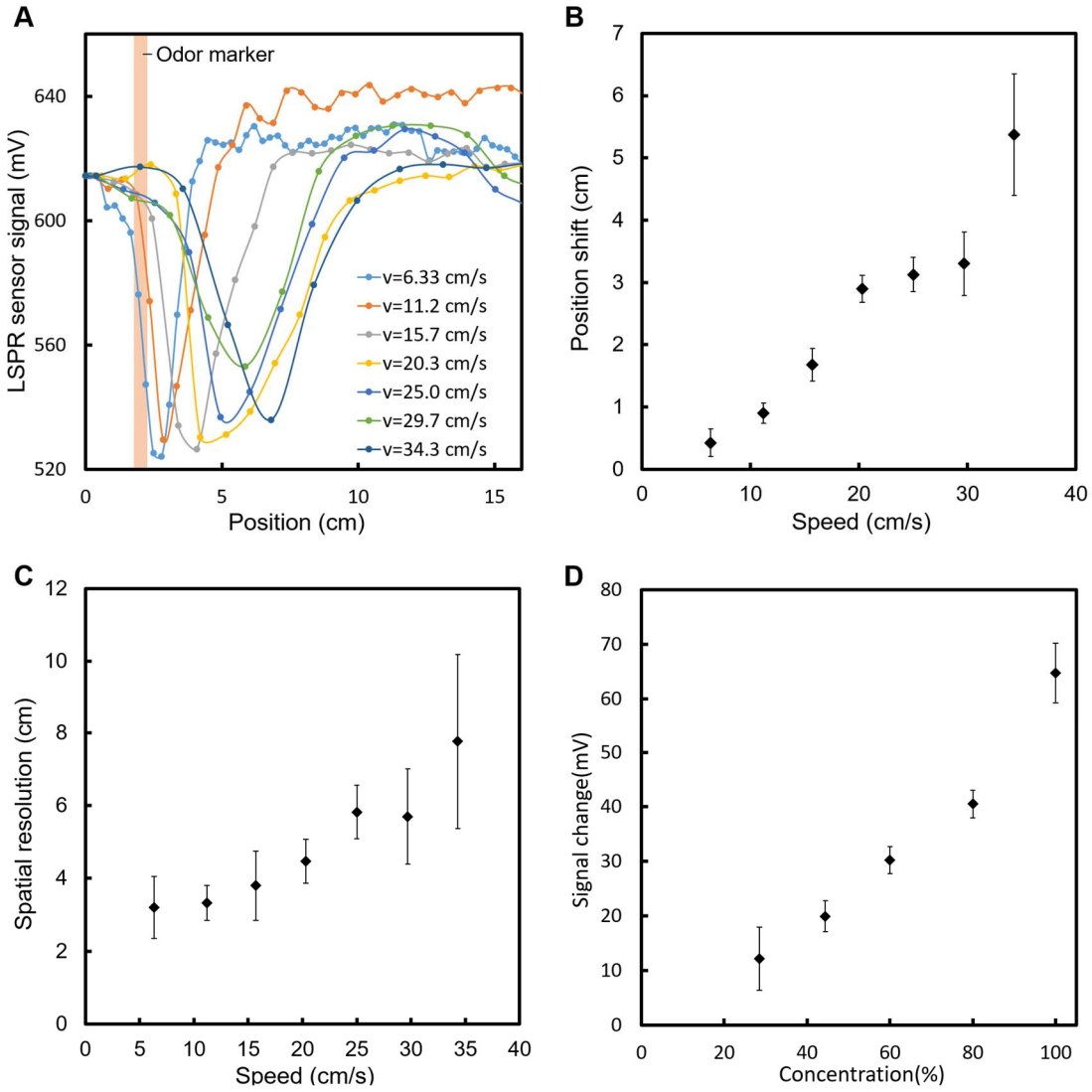

Figure 2. 9 Dependence of odor source detection characteristics on the travel speed of the robot. (A) Responses of the LSPR sensor module when passing the first gas source of course C at different speeds; travel speeds were set to 6.33, 11, 15.7, 20.3, 25, 29.7, and 34.3 cm/s. (B) Positional shift of gas sources when the robot had different travel speeds. (C) Spatial resolution based on a 50% valley for different travel speeds. (D) Sensor signal change when passing ethanol gas sources with different concentration. (n = 5).

2.3.3 Reading of digitized spatial odor information by the robot.

An odor barcode reading experiment was performed as a demonstration. A total of 34 pieces of paper were arranged, each with a length of 50 mm and a width of 5 mm (course C). Ethanol marks were made on the paper strips in the form of four eight-bit binary combinations to represent the word "ODOR" within the ASCII code framework. The first and last pieces of paper acted as marks of the start and end points. The distance between two adjacent pieces of paper at the start point and end point was set at 6 cm to

allow better recovery of the sensor. The distance between two adjacent pieces of paper except for the start point and end point was set at 2 cm because it has been confirmed that the LSPR gas-sensing module can accurately reflect the position of gas source at this distance. The pieces of paper that correspond to a value of "1" were marked with ethanol while those without ethanol corresponded to a value of "0" so as to create binary odor barcodes. The eight-bit binary combinations of 01001111, 01000100, 01001111 and 01010010 were arranged in order to represent the letters O, D, O and R, respectively.

The original output signal of the LSPR gas-sensing module is shown in Figure 2.10 for the robot passing the barcodes. The signals were obtained every 2 cm from the graph, while the start point and end point were recorded as "Start" and "End" signals. A series of signal values of the odor source was created to demonstrate how the system can obtain binary data from sensor signals. When the value increased more than the threshold ΔS between two adjacent signals, the robot moved away from the gas sources and the sensor output recovered to that for air. In that situation, the current position was marked with the value "0". When the value decreased more than ΔS, the robot moved towards the gas sources and the current position was marked with "1". When the change was within $|\Delta S|$, the robot was in the same condition as for the previous position. An up arrow, down arrow and right arrow in the figure respectively represent the sensor's recovery, response and holding. The translated binary combination was 01001111010001000100111101010010, which can be translated as the word ODOR according to ASCII code. With different kinds of binary combinations, the robot can record different kinds of digital information, such as a sign, a command or pictorial data, from the on-ground odor marker. The obtained results verified the proposed concept of a robot collecting spatial odor information from an invisible on-ground odor source.

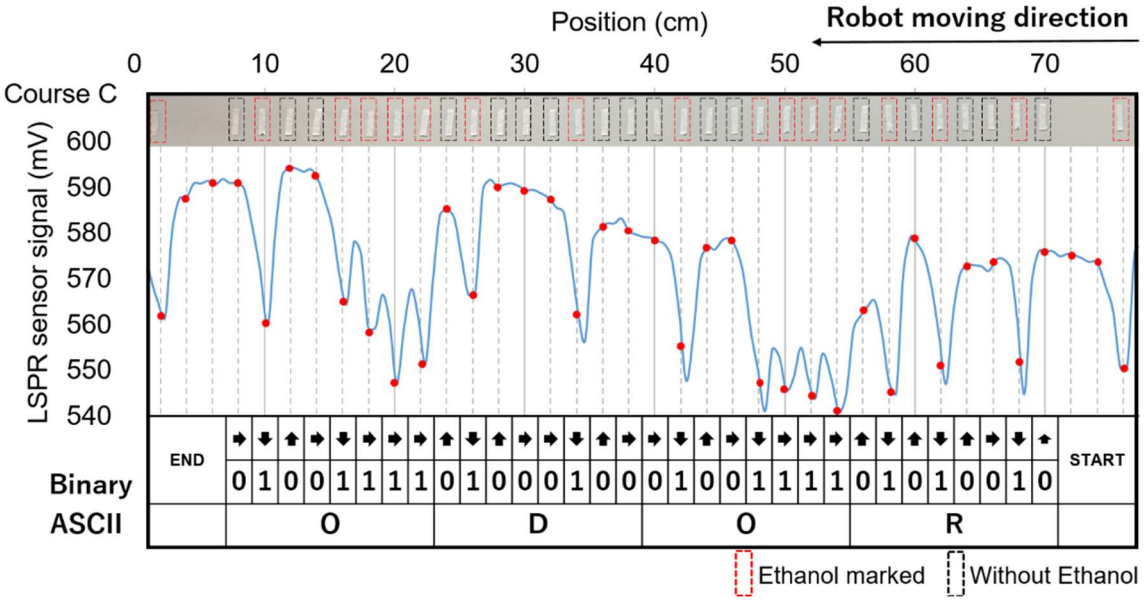

Figure 2. 10 Robot reading binary odor barcode information on course C. Red points on the sensor signal represent the sampling position every 2 cm. The down arrow represents the sensor responding to gas sources, and the up arrow represents the sensor signal recovering to its value for air, while the right arrow shows that the sensor is in the same condition as previously.

2.4 Conclusion

In this chapter, a high-speed LSPR gas-sensing module was developed and mounted on a robot for collecting spatial distribution information from on-ground odor traces while moving at a high speed. The sensor module could respond to ethanol/air switching at a high speed of more than 25 Hz and had a positive correlation with the gas concentration. The robot's capability to detect ethanol odor markers on the ground was evaluated in three different courses. Using the LSPR sensor module, the robot was able to accurately pinpoint the positions of odor sources with an accuracy on the order of several centimeters. Furthermore, the robot can scan invisible digitized spatial odor information (i.e., a barcode comprising ethanol-marked paper strips) at a high travel speed of 10 cm/s. The recorded eight-bit binary combinations could be translated to a human readable message under the ASCII standard. The proposed robot system has great potential for application in the field of odor spatial distribution detection.

Supporting information for chapter 2

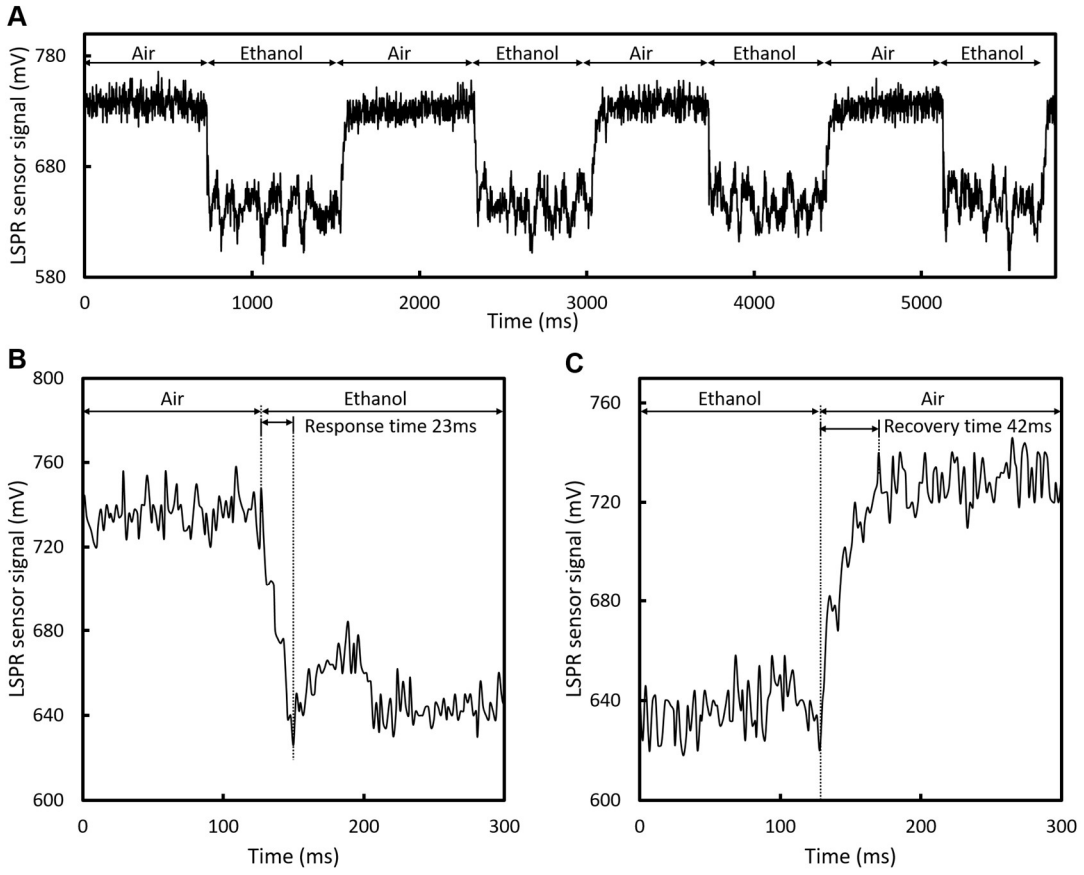

Figure S. 1 Sensing performance of LSPR gas sensor. (A)Response of LSPR gas sensor to a series of ethanol gas pulses. (B)Response time of LSPR gas sensor exposed with ethanol gas. (C)Recover time of LSPR gas sensor from ethanol gas exposing.

Reference

(1) Johnston, R. E. CHEMICAL COMMUNICATION IN RODENTS: FROM PHEROMONES TO INDIVIDUAL RECOGNITION. J. Mammal. 2003, 84 (4), 1141–1162.

(2) Amo, L.; Galván, I.; Tomás, G.; Sanz, J. J. Predator Odour Recognition and Avoidance in a Songbird. Funct. Ecol. 2008, 22 (2), 289–293.

(3) Lilienthal, A. J.; Loutfi, A.; Duckett, T., Airborne chemical sensing with mobile robots. Sensors 2006, 6 (11), 1616-1678.

(4) Ishida, H.; Wada, Y.; Matsukura, H., Chemical Sensing in Robotic Applications: A Review. IEEE Sens. J. 2012, 12 (11), 3163-3173.

(5) Loutfi, A.; Coradeschi, S. Smell, Think and Act: A Cognitive Robot Discriminating Odours. Auton. Robots 2006, 20 (3), 239–249.

(6) Farrell, J. A.; Pang, S.; Li, W. Chemical Plume Tracing via an Autonomous Underwater Vehicle. IEEE J. Ocean. Eng. 2005, 30 (2), 428–442.

(7) Deveza, R.; Thiel, D.; Russell, A.; Mackay-Sim, A. Odor Sensing for Robot Guidance. Int. J. Rob. Res. 1994, 13 (3), 232–239.

(8) Ishida, H.; Nakayama, G.; Nakamoto, T.; Moriizumi, T., Controlling a gas/odor plume-tracking robot based on transient responses of gas sensors. IEEE Sens. J. 2005, 5 (3), 537-545.

(9) Kowadlo, G.; Russell, R. A., Robot odor localization: A taxonomy and survey. Int. J. Rob. Res. 2008, 27 (8), 869-894.

(10) Ferri, G.; Caselli, E.; Mattoli, V.; Mondini, A.; Mazzolai, B.; Dario, P., SPIRAL: A novel biologically-inspired algorithm for gas/odor source localization in an indoor environment with no strong airflow. Rob. Auton. Syst. 2009, 57 (4), 393-402.

(11) Marques, L.; Nunes, U.; de Almeida, A., Olfaction-based mobile robot navigation. Thin Solid Films 2002, 418 (1), 51-58.

(12) Loutfi, A.; Coradeschi, S.; Lilienthal, A. J.; Gonzalez, J., Gas distribution mapping of multiple odour sources using a mobile robot. Robotica 2009, 27, 311-319.

(13) Neumann, P. P.; Asadi, S.; Lilienthal, A. J.; Bartholmai, M.; Schiller, J. H., Autonomous Gas-Sensitive Microdrone Wind Vector Estimation and Gas Distribution Mapping. IEEE Robot. Autom. Mag. 2012, 19 (1), 50-61.

(14) Ferri, G.; Jakuba, M. V.; Mondini, A.; Mattoli, V.; Mazzolai, B.; Yoerger, D. R.; Dario, P. Mapping Multiple Gas/Odor Sources in an Uncontrolled Indoor Environment Using a Bayesian Occupancy Grid Mapping Based Method. Rob. Auton. Syst. 2011, 59 (11), 988–1000.

(15) Hayes, A. T.; Martinoli, A.; Goodman, R. M. Distributed Odor Source Localization. IEEE Sens. J. 2002, 2 (3), 260–271.
(16) Hayes, A. T.; Martinoli, A.; Goodman, R. M. Swarm Robotic Odor Localization: Off-Line Optimization and Validation with Real Robots. Robotica 2003, 21(4), 427-441
(17) Marjovi, A.; Marques, L. Multi-Robot Olfactory Search in Structured Environments. Rob. Auton. Syst. 2011, 59, 867–881.
(18) Chen, Y.; Cai, H.; Chen, Z.; Feng, Q. Using Multi-Robot Active Olfaction Method to Locate Time-Varying Contaminant Source in Indoor Environment. Build. Environ. 2017, 118, 101–112.
(19) Mead, K. S. Using Lobster Noses to Inspire Robot Sensor Design. Trends Biotechnol. 2002, 20 (7), 276–277.
(20) Ando, N.; Emoto, S.; Kanzaki, R. Odour-Tracking Capability of a Silkmoth Driving a Mobile Robot with Turning Bias and Time Delay. Bioinspiration and Biomimetics 2013, 8 (1), DOI: 10.1088/1748-3182/8/1/016008016008.
(21) Kang, X.; Li, W. Moth-Inspired Plume Tracing via Multiple Autonomous Vehicles under Formation Control. Adapt. Behav. 2012, 20 (2), 131–142.
(22) Loutfi, A.; Broxvall, M.; Coradeschi, S.; Karlsson, L. Object Recognition: A New Application for Smelling Robots. Rob. Auton. Syst. 2005, 52, 272–289.
(23) Song, K.; Liu, Q.; Wang, Q. Olfaction and Hearing Based Mobile Robot Navigation for Odor/Sound Source Search. Sensors 2011, 11 (2), 2129–2154.
(24) Gonzalez-Jimenez, J.; Monroy, J. G.; Blanco, J. L. The Multi-Chamber Electronic Nose—An Improved Olfaction Sensor for Mobile Robotics. Sensors 2011, 11 (6), 6145–6164.
(25) Rodríguez, A. B.; Ramirez, A. R. G.; De Pieri, E. R.; Lopez, A. L.; de Albornoz, A. D. C. An Approach for Robot-Based Odor Navigation. J. Med. Biol. Eng. 2012, 32 (6), 453–456.
(26) Qiang Lu; Qing-Long Han; Xiaogao Xie; Shirong Liu. A Finite-Time Motion Control Strategy for Odor Source Localization. IEEE Trans. Ind. Electron. 2014, 61 (10), 5419–5430.
(27) Chen, Z.; Wang, J. Underground Odor Source Localization Based on a Variation of Lower Organism Search Behavior. IEEE Sens. J. 2017, 17 (18), 5963–5970.
(28) Li, J.-G.; Meng, Q.-H.; Wang, Y.; Zeng, M. Odor Source Localization Using a Mobile Robot in Outdoor Airflow Environments with a Particle Filter Algorithm. Aut. Robot 2011, 30, 281–292.

(29) Harvey, D. J.; Tien-Fu Lu; Keller, M. A. Comparing Insect-Inspired Chemical Plume Tracking Algorithms Using a Mobile Robot. IEEE Trans. Robot. 2008, 24 (2), 307–317.
(30) Cao, M.-L.; Meng, Q.-H.; Wang, J.-Y.; Luo, B.; Jing, Y.-Q.; Ma, S.-G. Learning to Rapidly Re-Contact the Lost Plume in Chemical Plume Tracing. Sensors 2015, 15 (4), 7512–7536.
(31) Schleif, F.-M.; Hammer, B.; Monroy, J. G.; Jimenez, J. G.; Blanco-Claraco, J.-L.; Biehl, M.; Petkov, N. Odor Recognition in Robotics Applications by Discriminative Time-Series Modeling. Pattern Anal. Appl. 2016, 19 (1), 207–220.
(32) Turduev, M.; Cabrita, G.; Kırtay, M.; Gazi, V.; Marques, L. Experimental Studies on Chemical Concentration Map Building by a Multi-Robot System Using Bio-Inspired Algorithms. Auton. Agent. Multi. Agent. Syst. 2014, 28 (1), 72–100.
(33) Bingham, J. M.; Anker, J. N.; Kreno, L. E.; Van Duyne, R. P., Gas Sensing with High-Resolution Localized Surface Plasmon Resonance Spectroscopy. J. Am. Chem. Soc. 2010, 132 (49), 17358-17359.
(34) Brigo, L.; Michieli, N.; Artiglia, L.; Scian, C.; Rizzi, G. A.; Granozzi, G.; Mattei, G.; Martucci, A.; Brusatin, G., Silver Nanoprism Arrays Coupled to Functional Hybrid Films for Localized Surface Plasmon Resonance-Based Detection of Aromatic Hydrocarbons. ACS Appl. Mater. Interfaces 2014, 6 (10), 7773-7781.
(35) Ghodselahi, T.; Zahrabi, H.; Saani, M. H.; Vesaghi, M. A., CO Gas Sensor Properties of Cu@CuO Core-Shell Nanoparticles Based on Localized Surface Plasmon Resonance. J. Phys. Chem. C 2011, 115 (45), 22126-22130.
(36) Mayer, K. M.; Hafner, J. H., Localized Surface Plasmon Resonance Sensors. Chem. Rev. 2011, 111 (6), 3828-3857.
(37) Hodgkinson, J.; Tatam, R. P., Optical gas sensing: a review. Meas. Sci. Technol. 2013, 24 (1), doi:10.1088/0957-0233/24/1/012004.
(38) Kreno, L. E.; Hupp, J. T.; Van Duyne, R. P., Metal-Organic Framework Thin Film for Enhanced Localized Surface Plasmon Resonance Gas Sensing. Anal. Chem. 2010, 82 (19), 8042-8046.
(39) Kajiura, M.; Nakanishi, T.; Iida, H.; Takada, H.; Osaka, T., Biosensing by optical waveguide spectroscopy based on localized surface plasmon resonance of gold nanoparticles used as a probe or as a label. J. Colloid Interface Sci. 2009, 335 (1), 140-145.
(40) Zhu, J.; Li, X. L.; Zheng, W.; Wang, B. A.; Tian, Y. B., Improved localized surface plasmon resonance index sensitivity based on chemically-synthesized gold nanoparticles

on indium tin oxide surfaces. Nanotechnology 2018, 29 (5), doi:10.1088/1361-6528/aa9c05.
(41) Yao, Y.; Ji, F. X.; Yin, M. L.; Ren, X. P.; Ma, Q.; Yang, J. Q.; Liu, S. F., Ag Nanoparticle-Sensitized WO3 Hollow Nanosphere for Localized Surface Plasmon Enhanced Gas Sensors. ACS Appl. Mater. Interfaces 2016, 8 (28), 18165-18172.
(42) Chen, B.; Liu, C. J.; Ota, M.; Hayashi, K., Terpene Detection Based on Localized Surface Plasma Resonance of Thiolate-Modified Au Nanoparticles. IEEE Sens. J. 2013, 13 (4), 1307-1314.
(43) Chen, B.; Mokume, M.; Liu, C. J.; Hayashi, K., Structure and localized surface plasmon tuning of sputtered Au nano-islands through thermal annealing. Vacuum 2014, 110, 94-101.
(44) Chen, B.; Liu, C. J.; Ge, L. P.; Hayashi, K., Localized surface plasmon resonance gas sensor of Au nano-islands coated with molecularly imprinted polymer: Influence of polymer thickness on sensitivity and selectivity. Sens. Actuators B Chem. 2016, 231, 787-792.
(45) Chen, Y. Q.; Lu, C. J., Surface modification on silver nanoparticles for enhancing vapor selectivity of localized surface plasmon resonance sensors. Sens. Actuators B Chem. 2009, 135

Chapter 3 Characteristics of odor trace visualization system with two-dimensional LSPR sensor

3.1 Introduction

In Chapter 2, the high response speed of the LSPR sensor module is demonstrated, and the ability of the robot equipped with this module to obtain distribution information from multiple on-ground odor traces with high spatial resolution while moving at high speeds.

However, the spatial distribution of chemical substances diffusing from odor traces continuously changes over time under the influence of the surrounding environment. It is a great challenge to describe the spatiotemporal distribution of these odor traces (1-4). Odor plumes and odor traces, while distinct, provide valuable insights into the spatiotemporal distribution of odor traces. An odor plume refers to the pattern of diffusion from the source, spreading out in a feather-like, fan shape, or irregular form. The plume's form and concentration change are influenced by environmental factors including wind speed and direction, temperature, and humidity. In environmental science and ecology, comprehending these odor plumes is vital for pinpointing and monitoring specific odor signatures, including those from pollutants (5-7). In contrast, odor traces refer to the residual trails left by a source on a surface, typically fading over time. This concept is vital in fields like forensic science, search and rescue, and animal behavior studies, where scent-tracking dogs are often employed (8-10). Specifically, the shape (spatial distribution) of an odor trace often intuitively indicates its source.

Sensing in both the spatial and temporal domains of odor traces is complicated. Researchers tried to use different kinds of gas sensors to capture this odor information. For example, the widely used MOX gas sensor, known for its sub-ppm sensitivity, affordability, and simplicity in fabrication (11). The application of mobile robot platforms equipped with this kind of gas sensors for odor source localization, employing specific tracking methodologies, epitomizes the use of spatial distribution data (concentration distribution) of an odor plume (12). However, two-dimensional sensing with MOX sensors relies on an array of multiple sensors, making them unsuitable for direct two-dimensional sensing. Moreover, these sensors are incapable of directly transforming sensitivity signals into visual formats for visualization, and their long recovery time

(several tens of seconds) makes it difficult in real-time detection. In contrast, biosensors, which can be deployed in a two-dimensional plane, allow for visual detection through fluorescent changes upon interaction with target substances. Recent advancements include camera-based imaging systems using gas-responsive materials for 2D gas visualization. Yoshioka et al. developed an odor imaging system based on multispectral fluorescence imaging, which visualized and discriminated components for a hand-shaped odor mark and airflow containing different odorants (13). Itani et al. developed a gas-imaging system using alcohol dehydrogenase for detection of the concentration distribution of acetaldehyde in breath and transdermal vapor (14). Despite their high sensitivity at ppb level, these biosensors are limited to detecting fluorescent-responsive substances and their long response times restrict real-time monitoring of odor trace changes.

Localized surface plasmon resonance (LSPR) is a phenomenon observed in nanomaterials, such as nanoparticles and nanorods, where electrons collectively oscillate in response to incident light (15). This resonance enhances the optical property change, like absorption of light at specific wavelengths. LSPR is highly sensitive to changes of permittivity of surrounding medium, such as the approach of gas molecules near the nanoparticles. LSPR is widely used in chemical sensors and biosensors based on optical signals (16-18). Controllable gold nano seeds can be fabricated by annealing a glass substrate sputtered with gold nanoparticles (19, 20). When AuNPs are irradiated with light, plasmons are excited and hot electrons are generated on the surface. As a result, Ag+ in the growth solution are reduced, and Ag nanoparticles grows on the surface of the Au nanoparticles. The growth of silver nanoparticles can be induced and controlled to form an Au/Ag core-shell structure through light exposure. The growth time can be adjusted to control the particle size and distance between nanoparticles to form different nano structure (21, 22). The fabrication technique for LSPR sensors shows its great potential as two-dimensional sensors and, owing to their ability to change optical characteristics in response to surrounding gas molecules, facilitate effective application for 2D odor trace visualization.

This chapter presents an odor trace visualization system based on a two-dimensional LSPR substrate. Au nanoparticles were fabricated on a glass substrate as nano seeds through a simple sputtering annealing method. Au/Ag core shell nanostructure was fabricated by Light introduced Ag growth on the surface of Au nanoparticles. Two-dimensional visualization images of an ethanol gas flow blown onto the substrate surface were obtained through changes in transmitted light. Visualization images of letter-shaped and strip-shaped odor traces were obtained through changes in reflected light. Moreover,

clear spatial distribution information (shape) of odor traces changing over time was obtained by differential images.

3.2 Experimental

Concept of odor trace visualization with two-dimensional LSPR gas sensing system

Figure 3.1a shows the concept of odor tracing robot with two-dimensional LSPR gas sensor. The optical property of LSPR substrate can be easily affected by the approach of gas molecules, changing the permittivity of surrounding media. This change in reflected and scattered light from LSPR substrate in ethanol atmosphere (the odor trace at the bottom) will be present on the sensor substrate and can be obtained by camera.

Fabrication of the two-dimensional LSPR gas sensing system

Figure 3.1b shows the components of the two-dimensional LSPR odor visualization system. It includes a LSPR substrate, an LED light source and a CCD camera (ML4022, FLI, New York, USA). The spectrum of light sources covers the resonance peak of Au and Ag nanoparticles. The intensity and angle of incident light source can be adjusted to obtain better image quality. The sensor film of the LSPR comprises a dual-layered metal nanoparticle structure, consisting of Au nanoparticles and Ag nanoparticles. As gas molecules from odor traces reach the LSPR sensor film, there is a direct change in optical characteristics, which is then captured by the CCD camera, acquiring the visualization images of the odor trace (Figure 3.2).

Fabrication of LSPR sensor substrate with Au/Ag core shell structure

A sputter method was used to fabricate a 5 nm Au nanoparticles layer on a glass substrate (100 mm × 100 mm × 0.5 mm) and then annealed at 580℃ for 10 h for size control and immobilization. Solutions of silver nitrate (10 mM, 5 mL), trisodium citrate (100 mM, 4 mL), and pure water (11 mL) were mixed together before light exposure. The substrate with the Au nano-island structure was immersed in the mixed solution and exposed to light from a halogen light source (MHF-150L, Moritex, Kanagawa, Japan) to provide the power of 2.0 mW/cm^2 to fabricate the Au/Ag core-shell nanostructure. The substrate was then washed with pure water and dried in nitrogen gas steam. Also, 9-h Ag growth sensor substrate was proved to have good sensitivity and lower transmittance for reflected type odor visualization system.

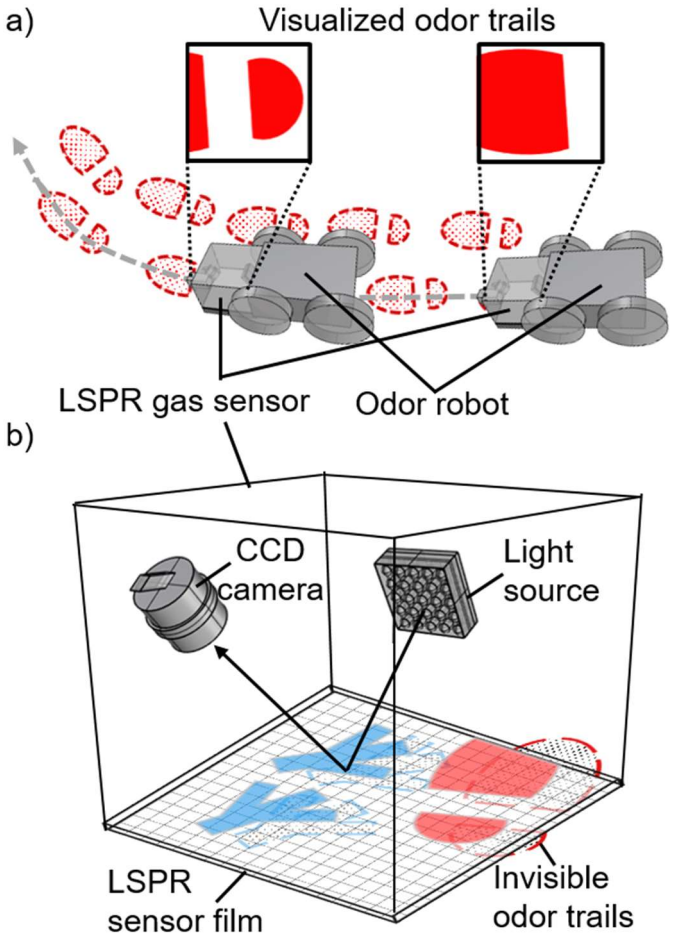

Figure 3. 1 Concept of odor tracing robot with two-dimensional LSPR gas sensor. (a) Odor tracking with visualized trace. (b) schematic of odor trails visualization system with LSPR sensor film

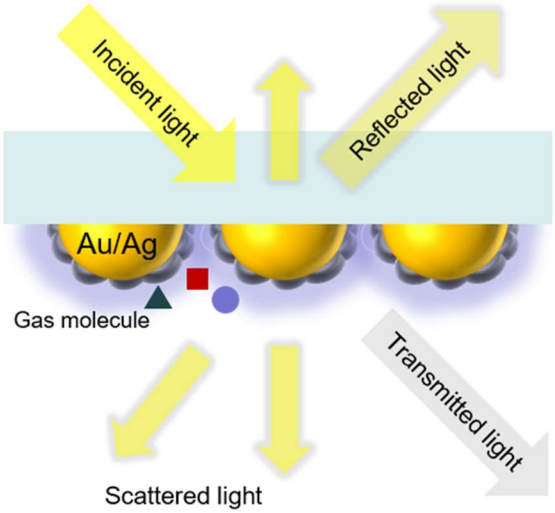

Figure 3. 2 Principle of LSPR gas sensing using reflected and transmitted light.

3.3 Result and discussion

3.3.1 Characterization of the Au/Ag nanostructure for LSPR gas visualization system.

Photograph of fabricated sensor film with 9h Ag growth is shown in figure 3.3A with the scanning electron microscope image (SEM) (FE-SEM, SU8000, Hitachi, Japan) of the surface structure of the Au/Ag nanoparticles in Figure 3.3B. Compared with Figure 2.4, the size of the nanoparticles after silver growth is significantly increased. These are caused by the growth of Ag nanoparticles on the surface of Au nanoparticles.

Figure 3.4A shows the transmittance change of the Au substrate with different Ag growth time with 3 h, 6 h and 9 h. the result shows a significant decrease in the transmittance in LSPR substrate with Ag growth time increased which represent that the Ag growth effectively reduce the transmittance light as a large noise.

In chapter 2.3.1, the SEM image of Au nano island structure on the glass substrate shows a particle size of about 30-40 nanometer. This nano island structure uniformly spread on the plane suggests that the substrate has the potential for high spatial resolution two-dimensional sensing, as each nanoparticle can be considered as an independent sensing unit. In this chapter, Au/Ag core shell nanostructure shows a particle size of about 50-80 nanometers, which can be considered as the spatial resolution of the LSPR sensor. When the LSPR substrate and CCD camera together form a two-dimensional visualization system, the spatial resolution of the visualized images obtained by the entire system can be considered as determined by the size of the substrate and the number of pixels in the camera, which is approximately Tens of micrometers, due to the high resolution of the LSPR substrate.

The substrates were exposed to ethanol gas to confirm their sensitivity change with Ag growth and the result is shown in Figure 3.4B. The response peak value of the 9-hour Ag substrate dropped to 4000 with the 3-hour growth Ag substrate has a 5000 response peak. This shows that Ag growth has a great influence on transmittance which can cut the noise and does not reduce the sensitivity of the substrate too much at the same time.

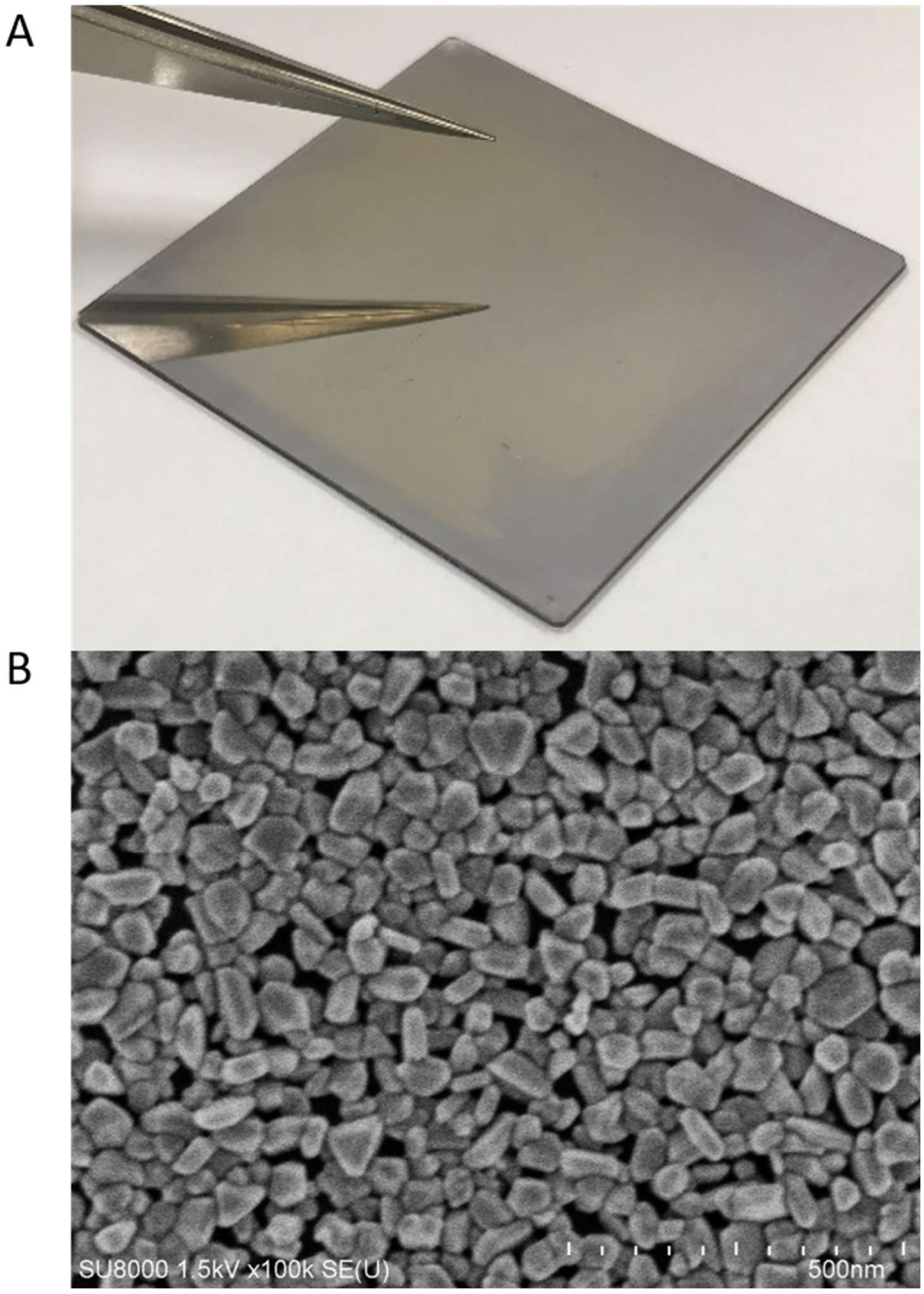

Figure 3. 3 Fabricated Au/Ag LSPR sensor substrate. (A) Photograph of Au/Ag LSPR sensor substrate. (B) SEM image of Au/Ag LSPR sensor substrate with 9-hour Ag growth.

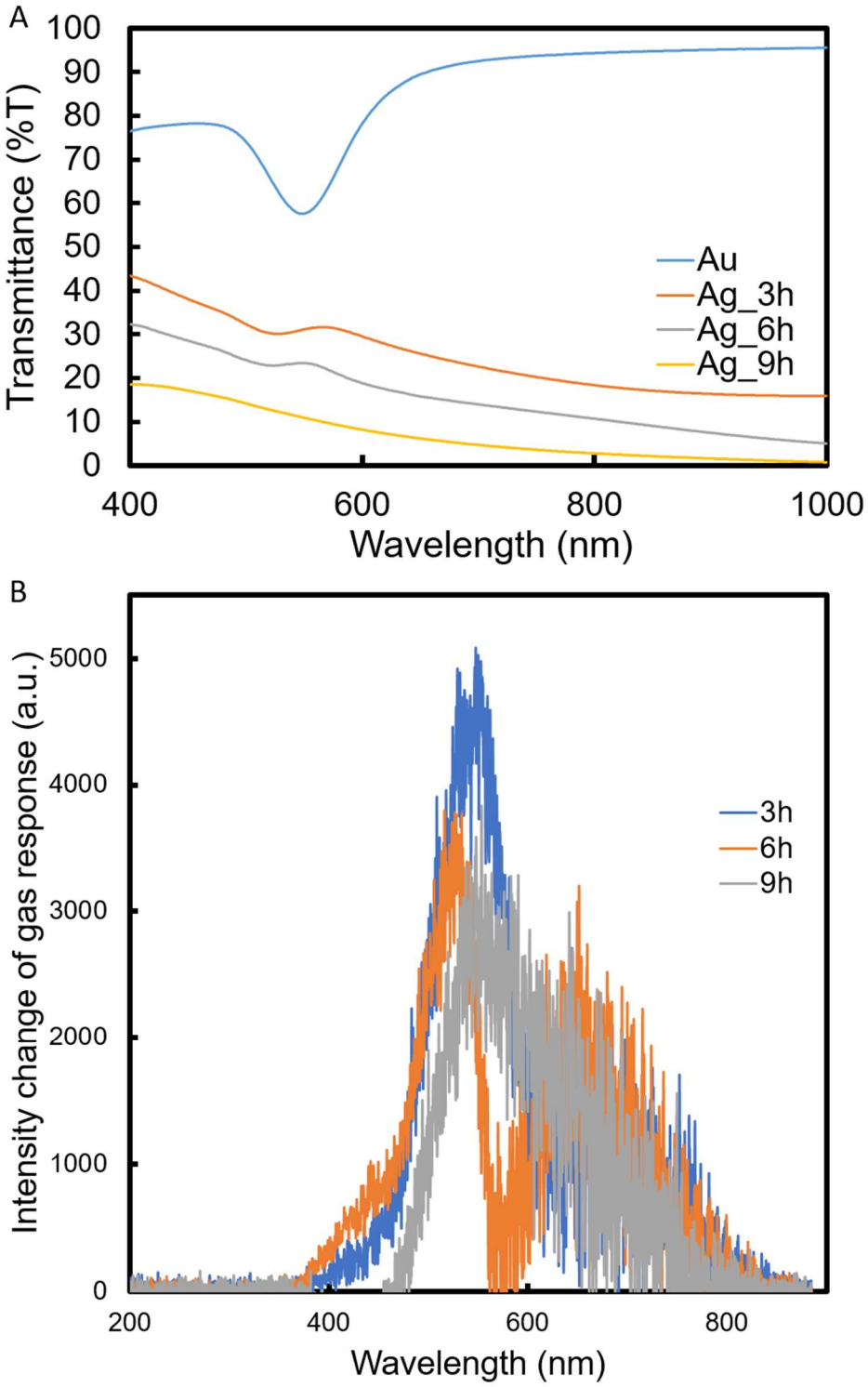

Figure 3. 4 Optical property of Au/Ag LSPR sensor substrate. (A) Transmittance change in Au/Ag substrate with different Ag growth time (0 h, 3 h, 6 h, 9 h). (B) Reflection variation of the Au/Ag LSPR substrate when exposed to air and ethanol gas.

3.3.2 Gas flow visualization with two-dimensional LSPR gas sensor (transmission type)

In the experimental setup, an ethanol gas stream was introduced from the bottom left corner of the LSPR substrate, while an air stream was blown directed from the middle of the substrate's bottom edge. Figure 3.5A shows the visualized gas image captured during the experiment, including a demarcated square area designated for analyzing the average change in transmitted light intensity. Figure 3.5B shows a cross-sectional plot representing the average changes in transmitted intensity across the substrate from Figure 3.5A, specifically measured 1 cm from the bottom edge. Additionally, Figure 3.6 shows the temporal change of transmitted light intensity in the captured image, recorded at 1.5-second intervals.

After starting the measurement, a notable flow of the low luminance area in the visualized image was observed as the ethanol gas flow rate increased (Figure 3.5A(a)→(b)) Furthermore, the introduction of the air stream from the bottom middle caused the ethanol gas stream to be blown away by the air steam ((b)→(c)). When the air stream stopped, the ethanol gas stream recovered to its original distribution ((c)→(d)). Figure 3.6 shows that the increase in the change of transmitted intensity value with the increase in the flow rate of the ethanol gas stream at 0 to 5 seconds and the decrease in the change value due to the blow of air at 5 to 10 seconds, changed in accordance with their time regions accurately.

The results indicate that the LSPR gas visualization sensor possesses a time resolution suitable for near real-time observation, enabling the acquisition of time change distribution information. Additionally, the transmitted intensity values of the ethanol gas stream before and after the introduction of the air stream were found to be remarkably similar, suggesting that the two-dimensional LSPR gas sensor exhibits excellent reversibility in gas visualization. This experiment demonstrates that the LSPR-based visualization gas sensor can accurately measure both spatial and temporal distribution information of gases. The utilization of this sensor facilitates the real-time acquisition of gas distribution data, highlighting its potential in various applications.

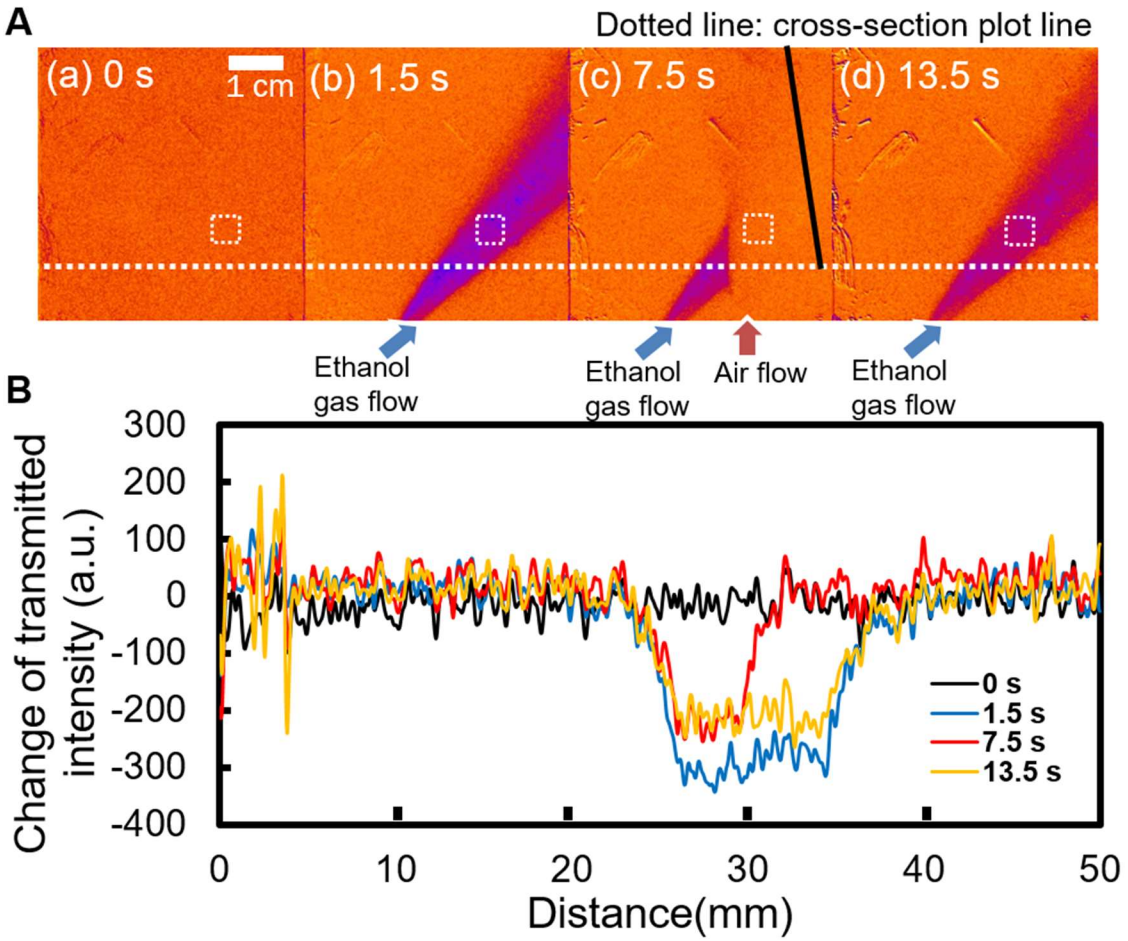

Figure 3. 5 Gas flow visualization with Au/Ag LSPR sensor substrate. (A) Visualization of gas spatial distribution with two-dimensional gas sensor: visual image of ethanol gas flow blown for 0 s (a), 1.5 s (b), 13.5s (d), Visual images of ethanol and air blown at the same time (d); (B) cross-section plot of grey value of (a-d) 1 cm from the bottom.

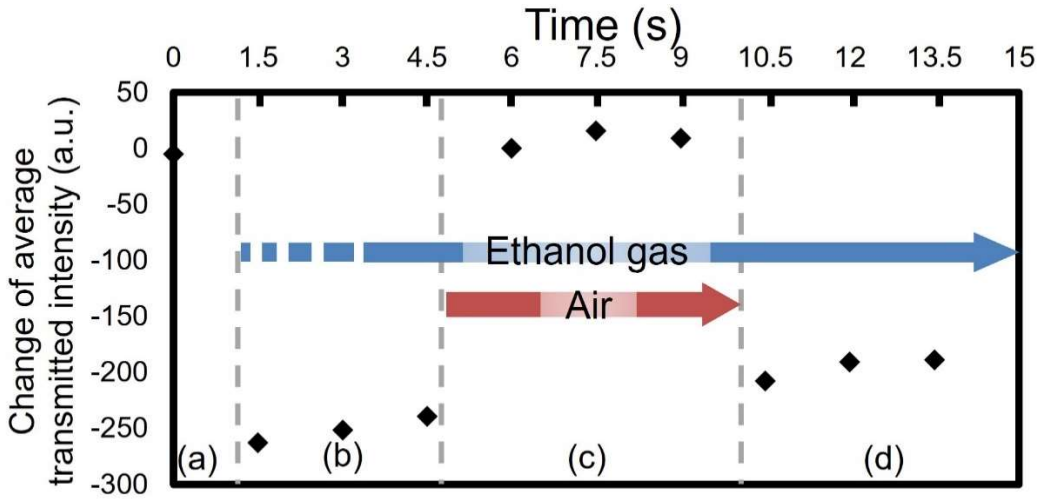

Figure 3. 6 Temporal change of average intensity value of selected area of captured picture.

3.3.3 Visualization of letter shape gas source with the sensor system (reflection type)

Figure 3.7 shows the experiment set up for letter shape gas source visualization with 9 h Ag growth substrate. Invisible odor trace shaped like letter "Q" and "U" written by ethanol solution was 1 mm below the LSPR sensor substrate, separately. an LED light source was positioned at a 45-degree angle relative to the substrate surface, while a CCD camera was aligned at a 90-degree angle to capture reflected light. The invisible "Q" and "U" have a total size of 4 cm ×4 cm and a line width of 3 mm, which is an indication for the sensor's high spatial resolution. The images were captured by CCD camera (exposure time 0.5 s) every 1 second. Background subtraction was applied during image processing to enhance visibility of the changes.

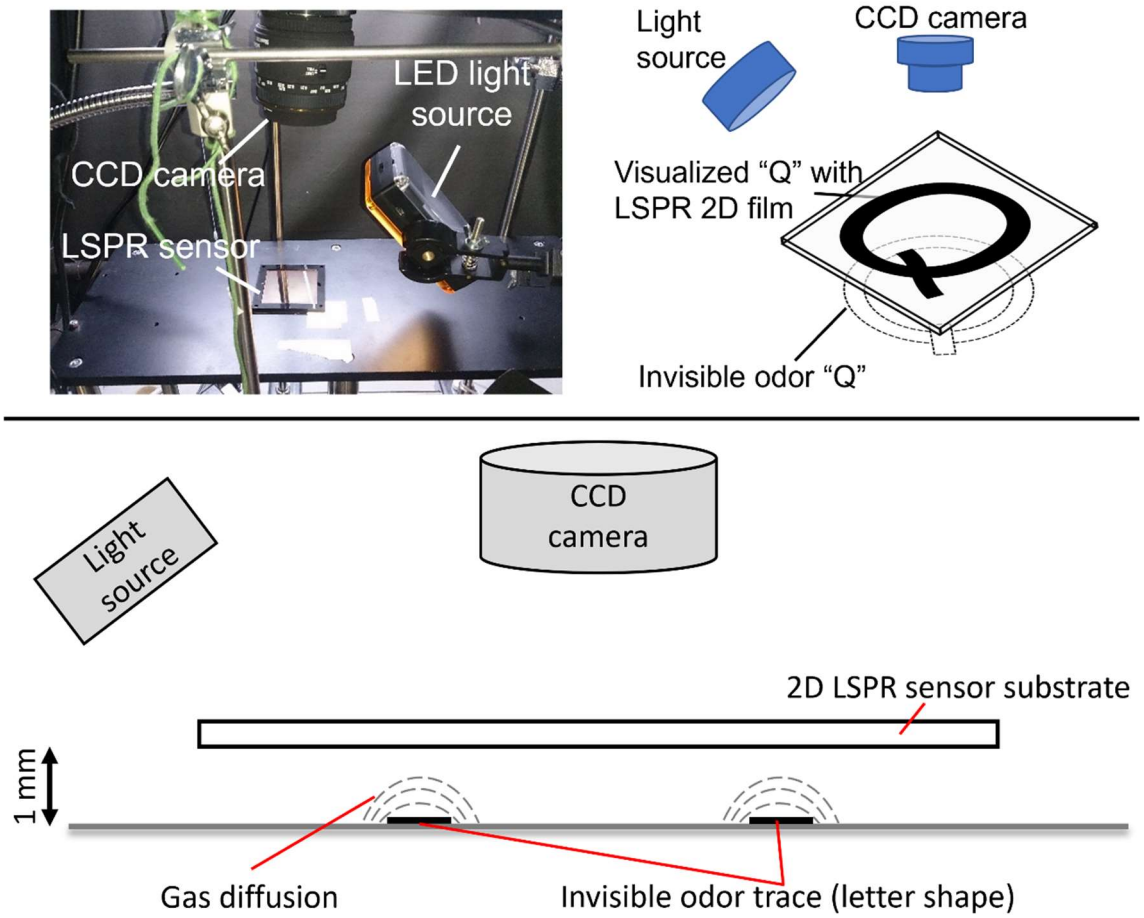

Figure 3. 7 Experiment set up and concept of letter shape gas source visualization. CCD camera and LED light source were placed 90-degree and 45-degree to the sensor substrate separately. Gas source was 1mm below the sensor substrate.

The result is shown in Figure 3.8. The odor source is more and more clearly imaged on the substrate over time, which may be due to the time required for gas to diffuse in a closed environment. The line width of visualized "Q" in Figure 3.8 are about 5 mm,

extended 1 mm to each direction compared with original odor trace, which shows a high reproducibility of the shape and distribution of odor source in this small scale. This indicated that the Au/Ag LSPR sensor has a far higher spatial resolution than array-type sensors using ordinary semiconductor gas sensors and can obtain the distribution of odor source by its shape at the same time. The temporal change of average intensity of five selected areas in “Q” from 0 s to 73.5 s is shown in Figure 3.9 for further investigation.

The intensity difference between the “Q” part and the central blank area increases significantly over time. This was attributed to the slow diffusion of ethanol gas in the confined space beneath the sensor substrate. This result suggests the sensor's suitability for continuous monitoring applications, such as in an odor tracing robot.

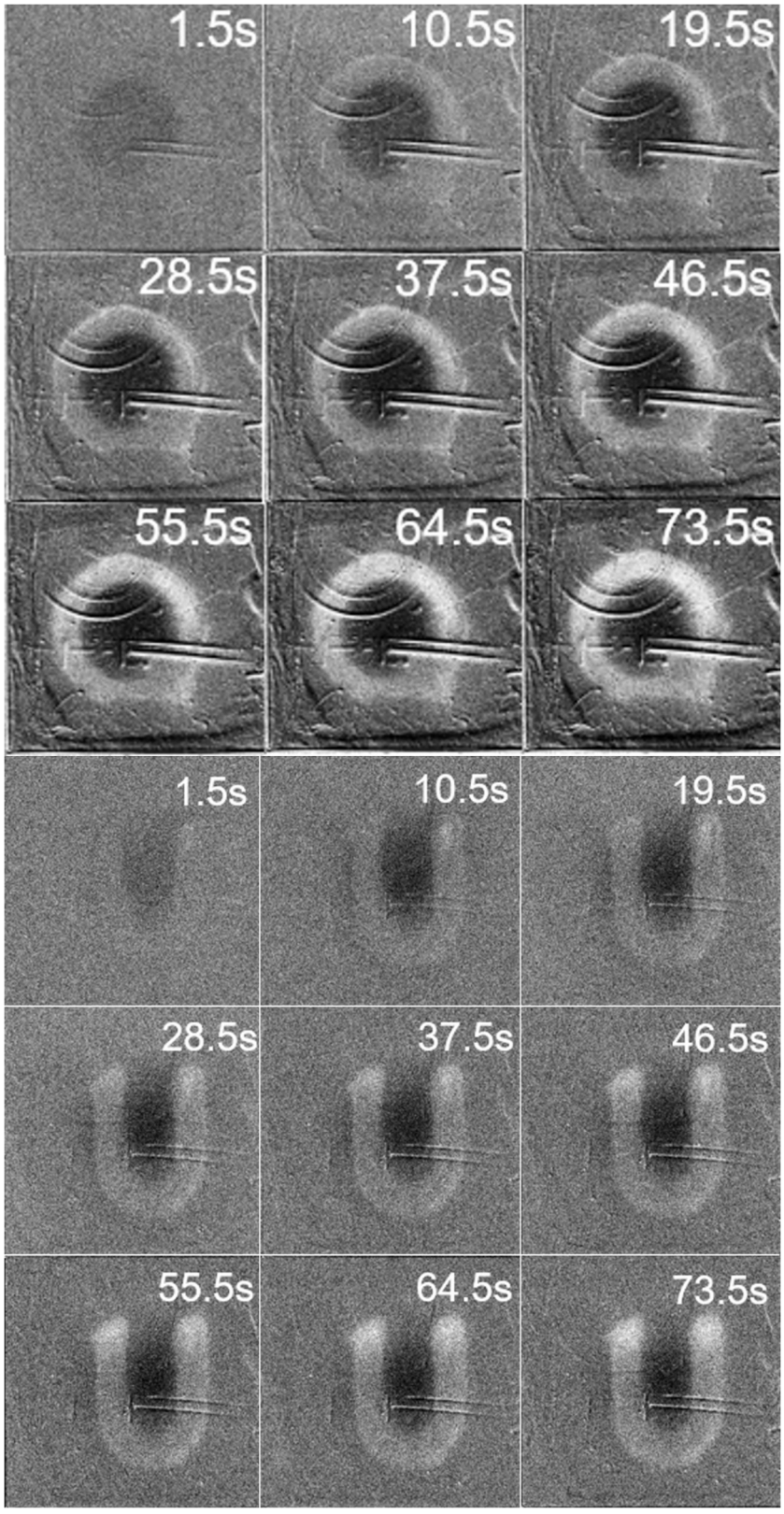

Figure 3. 8 Visualized odor source in shape of “Q” and “U”. Visualized images show the intensity change on LSPR substrate of odor source every 9 seconds.

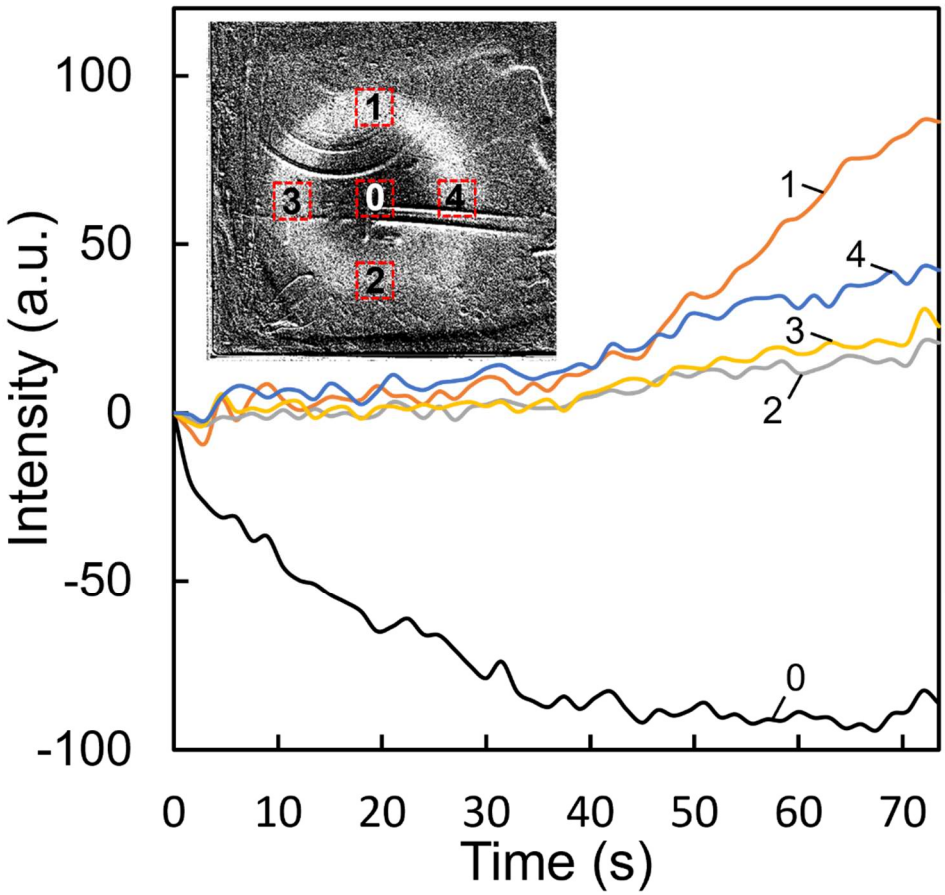

Figure 3. 9 Temporal change from 0 s to 73.5 s in the selected five areas(inset).

To further investigate the sensor's spatial resolution, a polypropylene masking sheet with four rectangular openings of varying widths (1 mm, 2 mm, 3 mm, and 4 mm) and a constant length of 20 mm was used to create strip-like odor sources. The experimental setup was shown in Fig. 3.10a. The distance between the sensor substrate and the odor source was approximately 2 mm. The differential images of visualized odor traces are shown in Fig. 3.10b. The images show that the visualized odor traces corresponding to the 2 mm, 3 mm, and 4 mm wide sources expanded beyond their actual sizes, whereas the trace for the 1 mm source just started to become visible. Temporal changes in the sensor's response to these four odor sources are shown in Fig. 3.10c. In this figure, a plot profile through the image's center generated by ImageJ, reveals that initially, sharp peaks appear at the odor sources position (e.g., at pixel 1000), later shifting towards the edges of the sources position. The intensity at the edges remains high, while other areas show some recovery after long time exposure.

The 1 mm width odor source was visualized later compared to the other three, with the 4 mm width source appearing earlier. This result suggests that the visualization speed is dependent on the size of the odor source. The most clearly observed peak,

corresponding to the 3 mm width odor trace, was used to calculate the imaging system's spatial resolution using the half-peak method mentioned in chapter 2. This result shows that when observing a 3 mm scale odor source, the sensor system can recognize between two independent odor traces at a distance of up to approximately 6 mm.

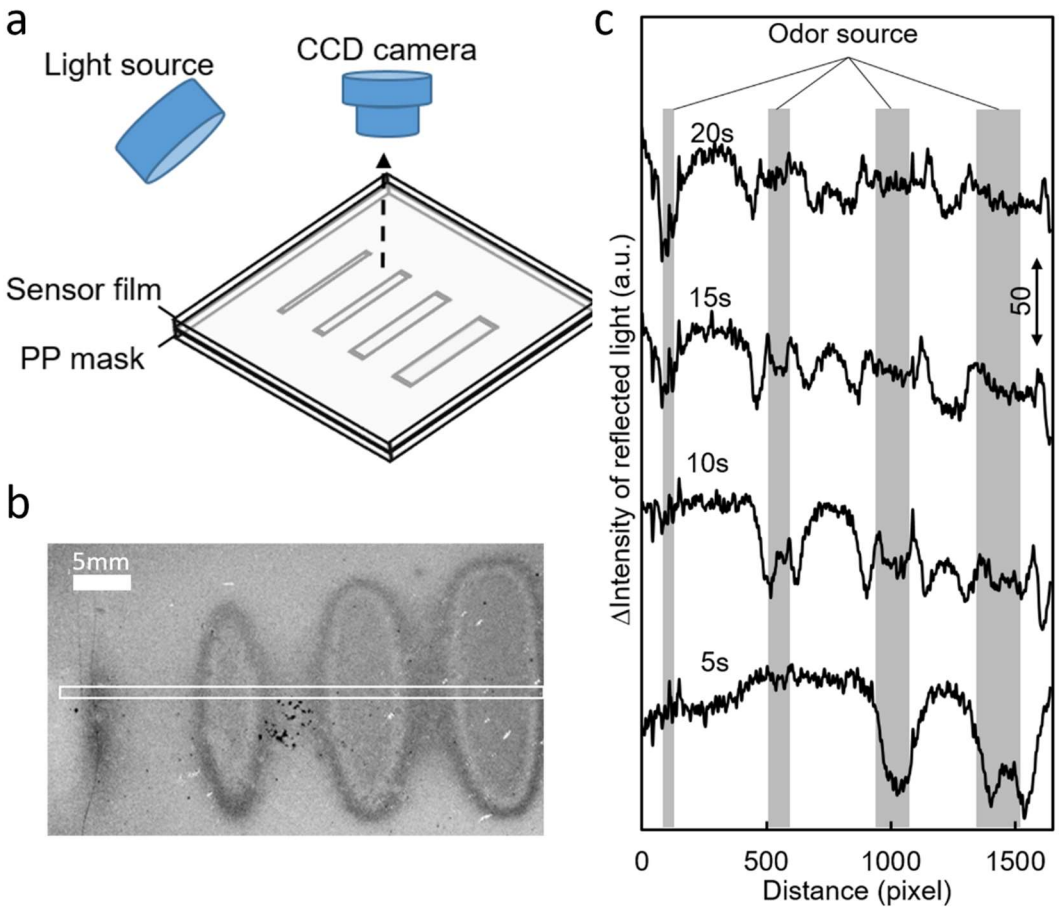

Figure 3. 10 Visualization of odor bar in different size. (a) Experiment up (b) differential images after 20 seconds exposed to ethanol. (c) Column average profile of reflected light intensity calculated from the selected area in (b).

3.4 Conclusion

In this chapter, a two-dimensional LSPR sensor substrate with Au/Ag core shell nanostructure was developed for visualization of spatial distribution information of odor traces. Ag growth on Au nanoparticles change the transmittance property but has less influence on the reflection property which was used as detection parameter in the experiment on reflection type. The spatial resolution of the substrate, determined by particle size and spacing, is tens of nanometers, while the spatial resolution of the visualization system, determined by the number of camera pixels, is tens of micrometers. The sensor system can detect the gas flow change with transmitted light change and

visualize odor traces with a 3 mm line width in letter shape of “Q” and “U” clearly with reflected light, which indicated the high spatial resolution of the sensor. The temporal change of the visualized part of odor traces showed a continuous change in intensity and can be expected for gas distribution change observation. The system's high response speed and high spatial resolution ensure that when it captures the spatiotemporal distribution of odor traces at close range, the changes in its images can be approximated as being determined by the natural diffusion of volatile odor substances.

Reference

(1) Nakamoto, T.; Ishida, H. Chemical sensing in spatial/temporal domains. Chem. Rev. 2008, 108, 680–704. https://doi.org/10.1021/cr068117e.

(2) Noziere, B.; Kalberer, M.; Claeys, M.; Allan, J.; D'Anna, B.; Decesari, S.; Finessi, E.; Glasius, M.; Grgic, I.; Hamilton, J.F.; et al. The Molecular Identification of Organic Compounds in the Atmosphere: State of the Art and Challenges. Chem. Rev. 2015, 115, 3919–3983. https://doi.org/10.1021/cr5003485.

(3) Marin, A.C.; Schaefer, A.T.; Ackels, T. Spatial information from the odour environment in mammalian olfaction. Cell Tissue Res. 2021, 383, 473–483. https://doi.org/10.1007/s00441-020-03395-3.

(4) Reddy, G.; Murthy, V.N.; Vergassola, M. Olfactory Sensing and Navigation in Turbulent Environments. Annu. Rev. Condens. Matter Phys. 2022, 13, 191–213. https://doi.org/10.1146/annurev-conmatphys-031720-032754.

(5). Kikas, T.; Ishida, H.; Webster, D.R.; Janata, J. Chemical plume tracking. 1. Chemical information encoding. Anal. Chem. 2001, 73, 3662–3668. https://doi.org/10.1021/ac0101813.

(6) Moore, P.; Crimaldi, J. Odor landscapes and animal behavior: Tracking odor plumes in different physical worlds. J. Mar. Syst. 2004, 49, 55–64. https://doi.org/10.1016/j.jmarsys.2003.05.005.

(7) Pearce, T.C.; Gu, J.; Chanie, E. Chemical source classification in naturally turbulent plumes. Anal. Chem. 2007, 79, 8511–8519. https://doi.org/10.1021/ac0710376.

(8) Thesen, A.; Steen, J.B.; Doving, K.B. Behavior of Dogs During Olfactory Tracking. J. Exp. Biol. 1993, 180, 247–251.

(9) Furton, K.G.; Myers, L.J. The scientific foundation and efficacy of the use of canines as chemical detectors for explosives. Talanta 2001, 54, 487–500. https://doi.org/10.1016/s0039-9140(00)00546-4.

(10) Ansari, A.A.A.; Aldajani, K.M.M.; AlHazaa, A.N.N.; Albrithen, H.A.A. Recent progress of fluorescent materials for fingermarks detection in forensic science and anti-counterfeiting. Coord. Chem. Rev. 2022, 462, 214523. https://doi.org/10.1016/j.ccr.2022.214523.

(11) Nikolic, M.V.; Milovanovic, V.; Vasiljevic, Z.Z.; Stamenkovic, Z. Semiconductor Gas Sensors: Materials, Technology, Design, and Application. Sensors 2020, 20, 6694. https://doi.org/10.3390/s20226694.

(12) Ishida, H.; Nakayama, G.; Nakamoto, T.; Moriizumi, T. Controlling a gas/odor plume-tracking robot based on transient re-sponses of gas sensors. IEEE Sens. J. 2005, 5, 537–545. https://doi.org/10.1109/jsen.2004.839597.

(13) Yoshioka, H.T.; Liu, C.J.; Hayashi, K. Multispectral fluorescence imaging for odorant discrimination and visualization. Sens. Actuators B-Chem. 2015, 220, 1297–1304. https://doi.org/10.1016/j.snb.2015.07.073.

(14) Iitani, K.; Sato, T.; Naisierding, M.; Hayakawa, Y.; Toma, K.; Arakawa, T.; Mitsubayashi, K. Fluorometric Sniff-Cam (Gas-Imaging System) Utilizing Alcohol Dehydrogenase for Imaging Concentration Distribution of Acetaldehyde in Breath and Transdermal Vapor after Drinking. Anal. Chem. 2018, 90, 2678–2685. https://doi.org/10.1021/acs.analchem.7b04474.

(15) Willets, K.A.; Van Duyne, R.P. Localized surface plasmon resonance spectroscopy and sensing. Annu. Rev. Phys. Chem. 2007, 58, 267–297. https://doi.org/10.1146/annurev.physchem.58.032806.104607.

(16) Jain, P.K.; Huang, X.H.; El-Sayed, I.H.; El-Sayed, M.A. Noble Metals on the Nanoscale: Optical and Photothermal Properties and Some Applications in Imaging, Sensing, Biology, and Medicine. Acc. Chem. Res. 2008, 41, 1578–1586. https://doi.org/10.1021/ar7002804.

(17) Badilescu, S.; Raju, D.; Bathini, S.; Packirisamy, M. Gold Nano-Island Platforms for Localized Surface Plasmon Resonance Sensing: A Short Review. Molecules 2020, 25, 4661. https://doi.org/10.3390/molecules25204661.

(18) Rodrigues, M.S.; Borges, J.; Lopes, C.; Pereira, R.M.S.; Vasilevskiy, M.I.; Vaz, F. Gas Sensors Based on Localized Surface Plasmon Resonances: Synthesis of Oxide Films with Embedded Metal Nanoparticles, Theory and Simulation, and Sensitivity Enhancement Strategies. Appl. Sci. 2021, 11, 5388. https://doi.org/10.3390/app11125388.

(19) Karakouz, T.; Tesler, A.B.; Bendikov, T.A.; Vaskevich, A.; Rubinstein, I. Highly Stable Localized Plasmon Transducers Obtained by Thermal Embedding of Gold Island Films on Glass. Adv. Mater. 2008, 20, 3893–3899. https://doi.org/10.1002/adma.200703092.

(20) Tesler, A.B.; Chuntonov, L.; Karakouz, T.; Bendikov, T.A.; Haran, G.; Vaskevich, A.; Rubinstein, I. Tunable Localized Plasmon Transducers Prepared by Thermal Dewetting of Percolated Evaporated Gold Films. J. Phys. Chem. C 2011, 115, 24642–24652. https://doi.org/10.1021/jp209114j.

(21) Yoshikawa, H.; Hironou, A.; Shen, Z.J.; Tamiya, E. Versatile Micropatterning of Plasmonic Nanostructures by Visible Light Induced Electroless Silver Plating on Gold

Nanoseeds. ACS Appl. Mater. Interfaces 2016, 8, 23932–23940. https://doi.org/10.1021/acsami.6b07661.

(22) Yin, Z.; Wang, Y.; Song, C.Q.; Zheng, L.H.; Ma, N.; Liu, X.; Li, S.W.; Lin, L.L.; Li, M.Z.; Xu, Y.; et al. Hybrid Au-Ag Nanostructures for Enhanced Plasmon-Driven Catalytic Selective Hydrogenation through Visible Light Irradiation and Surface-Enhanced Raman Scattering. J. Am. Chem. Soc. 2018, 140, 864–867. https://doi.org/10.1021/jacs.7b11293.

Chapter 4 Odor Trace Visualization System with a Two-Dimensional Backside Scattering LSPR Gas Sensor for mobile robot

4.1. Introduction

Collecting spatial information from odor traces, for example, the one-dimensional robot system mentioned in chapter 2, and obtaining visualized images of odor trace in 2D information in chapter 3. We have successfully visualized ethanol gas flow (using a transmissive type of detector) and letter “Q” and “U” shaped odor traces (using a reflective type of detector) using a 2D-LSPR substrate on a fixed experimental platform. However, the transmissive type of detector cannot detect odor traces on the ground, and the reflective type of detector captures the camera lens in the image and the strong reflection of its substrate interferes with subsequent image processing.

Chapter 2 demonstrated the high response and recovery speed of LSPR sensor. Chapter 3 demonstrated the high spatial resolution of two-dimensional odor trace visualization system with LSPR sensor. However, the ability of the visualization system to acquire the spatiotemporal distribution information of complex-shaped odor traces on the ground in real-world environments still remains to be developed.

In this chapter, a mobile odor trace visualization system based on an Au/Ag LSPR substrate was developed for visualization of on-ground odor traces to obtain its spatiotemporal change. The performance of the visualization system was enhanced through adjustments such as LSPR substrate placement, capture time and camera shooting angle to eliminate reflective noise. The reliability of visualizing odors spreading from on-ground odor traces was evaluated through a comparative experiment. Furthermore, by observing changes in the visualized images of the odor trace over time relative to the original shape of the odor trace, A method for reproducing the spatial distribution information of odor traces was established.

4.2. Experimental

4.2.1. Visualization Concept and Principle of the On-Ground Odor Trace Imaging System

Figure 4.1 shows the concept of the on-ground odor trace imaging system that visualizes the invisible realm of on-ground odor traces. These odor traces, imperceptible to the human eye, release volatile organic compounds (VOCs), and possess a unique two-dimensional spatial distribution (shape). The system is composed of three key components: a charge-coupled device (CCD) camera, a LSPR sensor substrate, and a LED light source. The core of the system is the LSPR substrate, which has a high response speed to VOCs and converts the chemical information of these compounds into optical information. The LSPR substrate consists of a glass substrate and noble metal nanostructures fabricated on its surface. The optical properties of the substrate can be changed by gas molecules from odor traces approaching the nanoparticles on the substrate. Variance in optical properties on the LSPR substrate presents a visual pattern, which can be captured by a CCD camera. The visualized images produced by this system accurately represents the shape of the invisible odor trace. This accuracy is achieved by positioning the substrate just a few millimeters away from the odor source. Essentially, the system translates the chemical information contained within the odor trace into discernible optical images, effectively converting invisible chemical phenomena into visually interpretable data. This bridge from the chemical to the visual domain opens new avenues for understanding and analyzing the subtle world of odor.

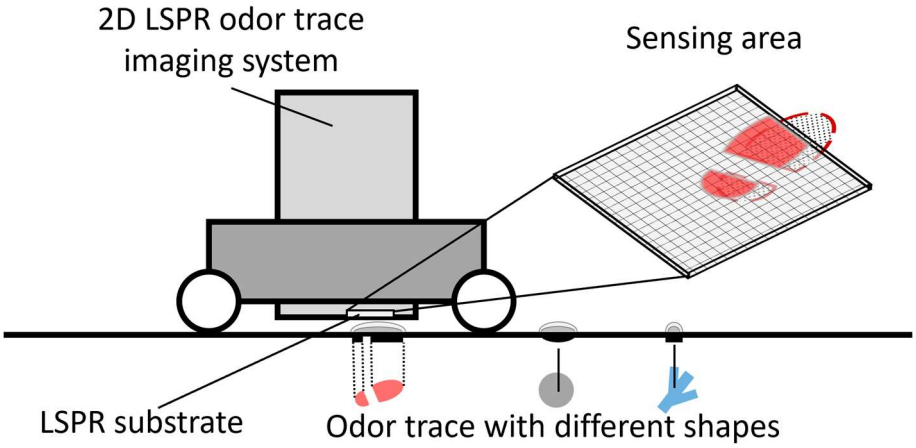

Figure 4. 1 Concept of collecting odor trace images (spatial information from an on-ground odor trace) with the two-dimensional (2D) localized surface plasmon resonance (LSPR) odor trace imaging system.

Figure 4.2 shows visualization principle of the system. The optical property of the substrate is determined by the absorption and scattering properties of the Au/Ag core-

shell nanostructure on its surface. These characteristics are closely linked to the nanostructure's size, shape, and the dielectric properties of the surrounding environment. When gas molecules approach the nanostructure, they influence the surrounding dielectric environment and/or the chemical nature of the surface of the nanostructure. Such changes in the dielectric properties of the surrounding media result in changes to the light scattering from the LSPR sensor surface, which can be observed and visualized using a CCD camera from the backside. The intensity of scattered light (S) is calculated as:

$$S = I - R - T - A, \tag{1}$$

where I represent the intensity of incident light, R is the intensity of reflected light, T is the intensity of transmitted light, and A is the intensity of absorbed light.

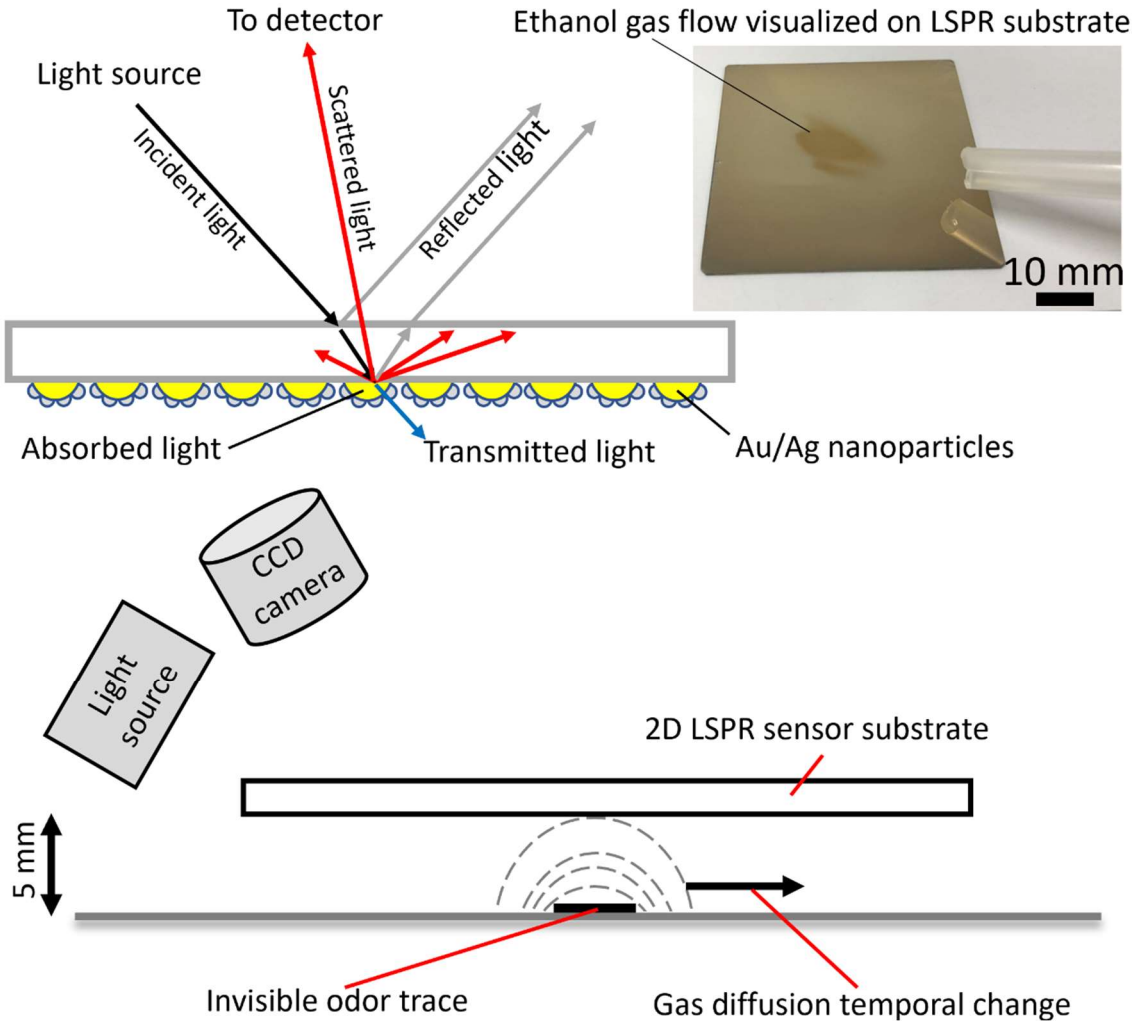

Figure 4. 2 Visualization principle of the odor trace imaging system with an Au/Ag core-shell LSPR substrate that is based on changes in scattering and absorption captured by a charge-coupled device (CCD) camera when gas molecules approach the Au/Ag nanoparticles.

The visualized image of ethanol gas flow blown onto the LSPR substrate is shown in the right top of Figure 4.2. The chemical information of an ethanol gas flow is converted into changes in intensity (optical information) by the LSPR substrate and then captured by the CCD camera. Meanwhile, owing to the substrate's high response/recovery speed, it can recover to its original state once the ethanol gas disappears, leading to a response/recovery in the surrounding dielectric environment, such that the substrate can effectively record a rapidly changing gas environment.

4.2.2. Fabrication of an LSPR Sensor Substrate with an Au/Ag Core-Shell Nanostructure

Silver nitrate and trisodium citrate were purchased from Wako, Japan.

Au nano seeds were fabricated on a glass substrate with dimensions of 50 mm × 50 mm × 1 mm. Firstly, the substrate underwent a cleaning process using pure water, acetone, and ethanol, in an ultrasonic cleaner, followed by drying with a stream of nitrogen gas. The glass substrate was then placed in a sputter machine (SC-701HMC II, Sanyu Denshi, Tokyo, Japan) for Au nanoparticle deposition through sputtering at 20 mA for 8 s. An annealing treatment was conducted in a programmable electric furnace (SMF-1, As One, Osaka, Japan) at 580 °C for 8 h to fabricate an Au nano-island structure on the glass substrate.

For the growth of Au/Ag core-shell nanostructure, a mixed solution of silver nitrate (10 mM, 5 mL), trisodium citrate (100 mM, 4 mL), and pure water (11 mL) were prepared before light exposure. The substrate with the Au nano-island structure was immersed in the mixed solution and exposed to light from a halogen light source (MHF-150L, Moritex, Kanagawa, Japan) to provide the power of 2.0 mW/cm^2 for Ag growth. The substrate was washed with pure water and dried under a nitrogen gas steam.

4.2.3. Fabrication of a 2D LSPR Odor Trace Imaging System

Figure 4.3 shows the photograph of the 2D LSPR odor trace imaging system.

The frame of the imaging system is made of aluminum alloy and has dimensions of 30 cm × 20 cm × 50 cm. The device's height is adjustable to maintain the LSPR substrate's measuring area in close distance to the odor trace in different experimental environments. The imaging system is covered with black cardboard to avoid the influence from ambient light. A CCD camera (ML4710-1-BB, FLI, New York, NY, USA) is set at the top of the sensor chamber to capture changes in intensity on the sensor substrate. A square hole is created in the chamber floor 15 cm below the camera for the placement of the LSPR sensor substrate. An LED light source (Ulanzi 96 LED Video Light, Ulanzi, Shenzhen, China) is set at the left side of the chamber. The angle between the light source and

substrate is set at about 30 degrees to avoid direct reflection. The wavelength range of the LED light source is 400 nm to 800 nm with its peak at 600 nm. An ice pack is placed next to the substrate to suppress the desorption of gas molecules on the substrate surface due to the internal temperature of the chamber being higher than the external temperature, a condition caused by heat dissipation from the camera.

4.3. Results and Discussion

4.3.1. Characterization of the Au/Ag Core-Shell LSPR Substrate

Figure 4.4a shows both SEM images of the nanostructure on the surface of the substrate and photographs of Au and Ag nanoparticle growth for 3, 6, and 9 h. The substrate color transition from pink to dark brown as the Ag growth. The SEM image of the Au nanoparticle substrate shows a dispersed island nanostructure, with particle sizes ranging from 10–30 nm. The diameter of the nano-islands increases to approximately 50 nm as Ag growth, and the distance between the islands decreases, resulting in a denser structure.

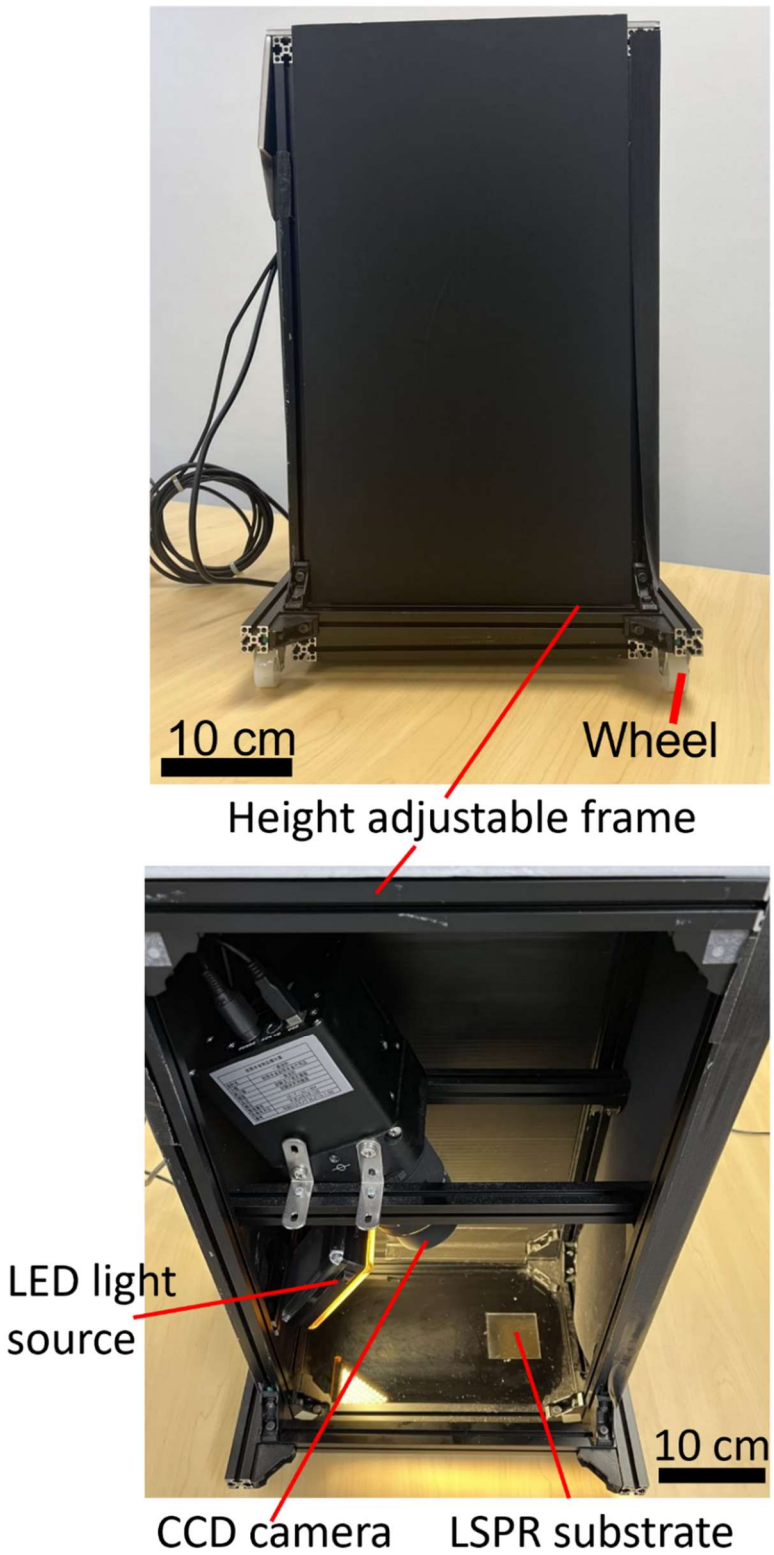

Figure 4. 3 Overview of the 2D LSPR odor trace imaging system (top) and photograph of the imaging system (bottom), comprising a CCD camera, light-emitting diode (LED) light source, and LSPR sensor substrate.

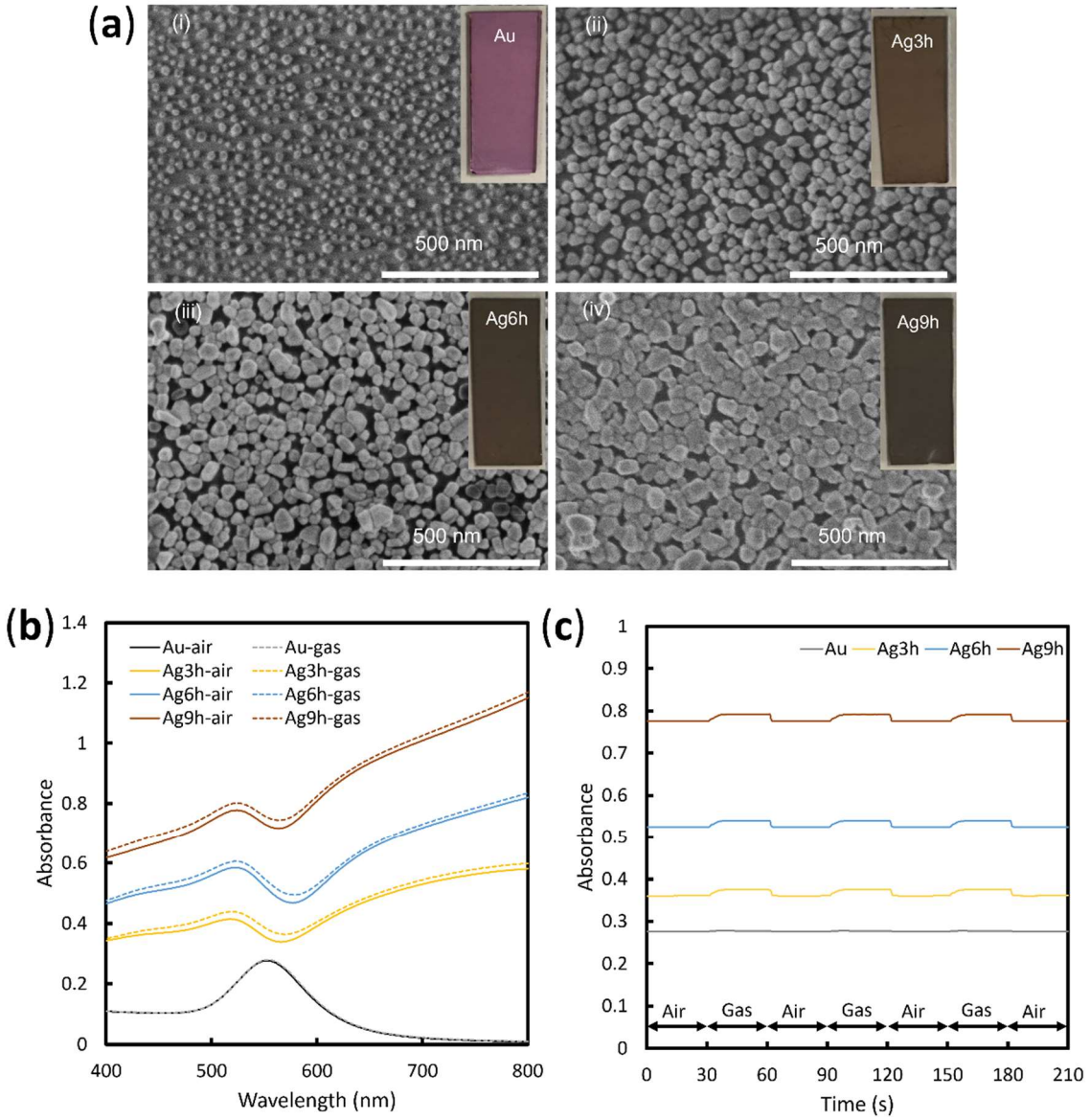

Figure 4. 4 Characteristics of the LSPR sensor substrate. (a) Scanning electron microscope image of the Au/Ag core-shell nanostructure. (i) Au nanoparticles only. (ii)–(iv) Au nanoparticle layers with growth at different times. (Insets) Photographs of the LSPR sensor substrates (b) Absorption spectra of the LSPR substrates exposed to air and ethanol gas. (c) Absorbance changes when the LSPR substrates were exposed to air and ethanol gas.

Figure 4.4b shows the absorption spectra of each substrate under conditions of air exposure and saturated ethanol gas exposure. The solid line represents the absorption spectrum in air, whereas the broken line corresponds to the spectrum under ethanol gas exposure. With Ag growth, the absorption of visible light by the substrate increases and the intensity of transmitted light correspondingly decreases. This result shows that the Au/Ag core shell structure effectively reduces the effect of transmitted light from outside on imaging when used in the 2D imaging system.

To evaluate influence of Ag nanoparticles growth on substrate sensitivity, the substrates were exposed to air and ethanol gas switching environment at 30 second intervals. Figure 4.4c shows the absorption changes at 550 nm for substrates at different stages of Ag growth: Au nanoparticle substrate and substrates after 3, 6, and 9 hours of Ag growth, with absorption changes recorded at 0.002, 0.015, 0.015, and 0.016, respectively. This indicates an enhancement in substrate sensitivity attributable to Ag growth, alongside a maintained stability in absorbance change. The absorbance spectrum's red-shifted shoulder (Figure 4.4b) results from a resonance generated by coupling between the nanoparticles (2). The result shows that Ag growth effectively suppresses noise from transmitted light without compromising sensitivity.

Prior research shows that the optical properties of LSPR substrates can be adjusted through controlled light exposure (i.e., growth time) (3). Although it is not able to create exactly identical LSPR substrates, those obtained with the same exposure time exhibit similar optical characteristics. As the reverse growth of controlled Au on Ag seeds is not achievable in this fabrication process, the susceptibility of the Ag shell to oxidation remains a challenge during data collecting. To reduce the influence of Ag oxidation on the experimental results, all data were collected within one week after preparation of LSPR substrates.

4.3.2. Comparative Experiment of the Visualization of an A-Shaped Odor Trace

As the optical properties of the LSPR substrate do not simply represent its performance in the odor trace imaging system, a comparative experiment was conducted for further analysis and evaluation. The LSPR substrate's response is significantly influenced by environmental changes such as temperature, humidity, and ambient light. Therefore, the experiment is thus designed to accurately obtain the differences in imaging results between the LSPR substrate and non-LSPR substrate under the same conditions for the same odor trace.

The odor trace imaging system shown in Figure 4.3 was placed in a dark room. Two glass substrates, each with dimensions of 25 mm × 50 mm, were fabricated with a 5-nm Au layer and Ag growth for 9 h. The two substrates were placed on a poly(methyl methacrylate) (PMMA) frame, with the Au/Ag core-shell nanostructured side of left substrate facing downwards (sensor side) and the glass side of the other substrate also oriented downwards for a comparative experiment. As shown in Figure 4.5a, black cardboard with dimensions of 5 cm × 5 cm, treated with a hydrophobic solvent (Fluoro Surf, Fluorotech, Kasugai, Japan) outside an “A” shape area and dried for 10 min, was

coated within the “A” shape with 95% ethanol solution to create an A-shaped odor trace immediately before imaging. The LSPR sensor substrate was positioned approximately 4–5 mm above the odor trace. The ethanol gas concentration directly above the odor trace at a distance of 5 mm, was approximately 7000 ppm, measured by a PID sensor (Phocheck+, Ion Science, Fowlmere, UK).

The CCD camera was set to capture 200 images every 0.9 seconds over roughly 230 seconds with an exposure time of 0.25 seconds, recording the intensity changes on both the LSPR and glass substrates induced by the A-shaped odor trace. After background subtraction with the first image as the reference image, differential images with a clear view of intensity changes were obtained and shown in Figure 4.5b. Initially, there was little to no observable change on both substrates within the first 57.5 seconds. By approximately 115 seconds, a slight intensity reduction was noted on the sensor side, leading to the gradual appearance of the "A" shape by around 140 seconds, and fully visible by approximately 200 seconds. In contrast, there were hardly any notable changes on the glass side during the capturing process. The overall change in intensity over time was clearer on the sensor side than on the glass side. It is speculated that the diffusion of ethanol gas resulted in the formation of a concentration gradient, extending from areas of high to low concentration. This gradient significantly influenced the substrate's absorption and scattering characteristics, as detected by the CCD camera.

To further investigate the difference between the sensor side and the glass side, the intensity profile for specified area (Figure 4.5c) was plotted using ImageJ software (V 1.52a), with a 20-pixel line width, as shown in Figure 4.5d. The line width of the profile is set in the longitudinal direction, and the average intensity over 20 pixels in the transverse direction is presented. The gray bar shows the position of the interface between the sensor side and the glass side. At approximately 3 and 7 mm to the left of the interface line on the sensor side, two clear valleys were observed, corresponding to the A-shaped odor trace. In contrast, at the corresponding positions on the glass side, there is hardly any change in intensity. This intensity profile on the two substrates area effectively shows the difference in intensity changes due to the odor trace on the LSPR substrate and glass substrate under the same external environmental condition over time. The result shows that the parts of the cardboard with and without the odor trace show differences on the substrate, creating a boundary. In the differential images, these differences produce a visible line which can reveal the shape of the original odor trace.

Figure 4.5e shows the average differential intensity changes over time for both sides (sampling areas shown in inset image). the sensor side exhibited a notable normalized intensity change of 80 within approximately 160 seconds, whereas the glass side showed

a minor change of 20. At the location of the odor trace, owing to the diffusion of saturated ethanol gas that affects the optical properties of the substrate in the sampling area, the average intensity change increases over time. Meanwhile, the intensity change over time for the glass substrate serves as a background of environmental influences.

In previous research, Au/Ag LSPR substrates were employed for visualizing various volatile gases volatile gases, including geraniol, pentadecane, piperitone, and eugenol (4). This experiment advances the capability to capture spatial distribution information (shape) and temporal changes of complex-shaped ethanol odor traces, demonstrating the LSPR substrate's enhanced sensitivity and specificity in odor trace imaging.

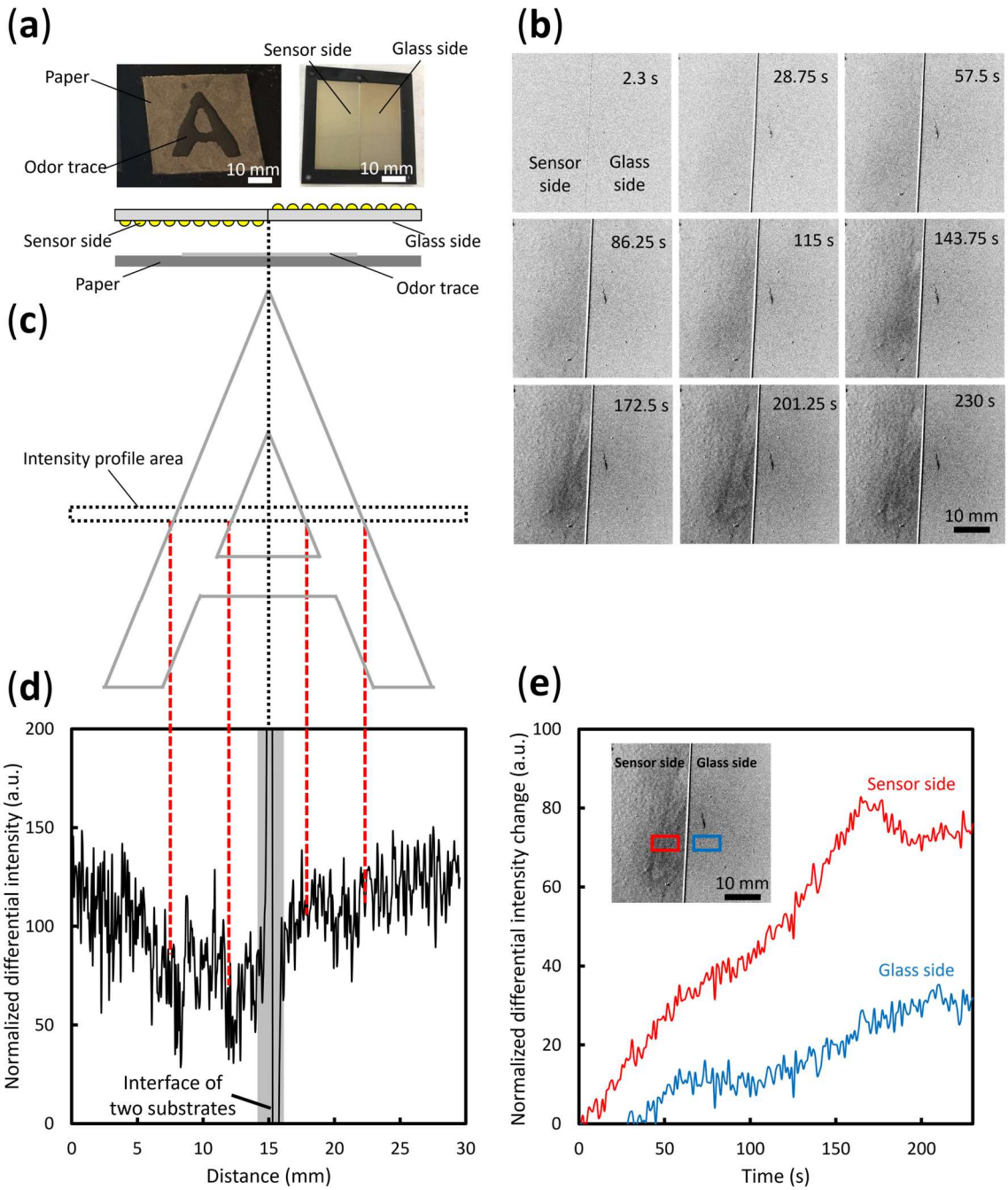

Figure 4. 5 Comparative experiment of odor trace visualization. (a) Experiment set up. (b) Differential images of the A-shaped odor trace on LSPR and non-LSPR substrates over time. (c) Intensity profile area. (d) Intensity changes on both sensor side and glass side in the differential image at 230 s. (e) The average change in intensity between the sensor side and glass side over time. The inset shows the two sampling areas.

4.3.3. Indoor Environmental On-Ground Star-Shaped Odor Trace Visualization

Performance of the imaging system to capture shape information of on-ground odor trace was evaluated in an indoor environment at room temperature, as shown in Figure 4.6a.

A black mark was applied to indicate the sampling position of the imaging system before moving the system onto the carpet used in the experiment, ensuring that the LSPR sensor substrate was directly above the odor trace during the imaging process. A star-shaped hole was created in a PMMA substrate with dimensions of 50 mm × 50 mm × 2 mm, serving as a mask. The star opening's overall dimension was approximately 15 mm × 15 mm, with the distance from the center to each of the five exterior vertices being 7.8 mm, and to each of the interior vertices being 3.9 mm. The mask was placed on the carpet, and the space between the carpet and the PMMA mask was saturated with ethanol solution to create a star-shaped odor trace, as shown on the right of Figure 4.6a. The distance between the odor trace and LSPR substrate was adjusted to approximately 4–5 mm. The exposure time of the CCD camera was set to 0.5 second, capturing 100 images at intervals of approximately 0.88 second over a period of approximately 138 seconds.

The different directions in the original star shape were marked with arrow to describe the different directions in the visualized images. As shown in Figure 4.6b, starting from the left side, the five exterior vertices were sequentially labeled as exterior vertices 1 to 5 and the five interior vertices were labeled as interior vertices 1 to 5. Ten line arrows extending from the center of the star to the five exterior vertices and five interior vertices, were marked as line arrows V1 to V5 and C1 to C5, to investigate the intensity change in different directions of the image. The length of each line was approximately 15 mm (i.e., 250 pixels in the image).

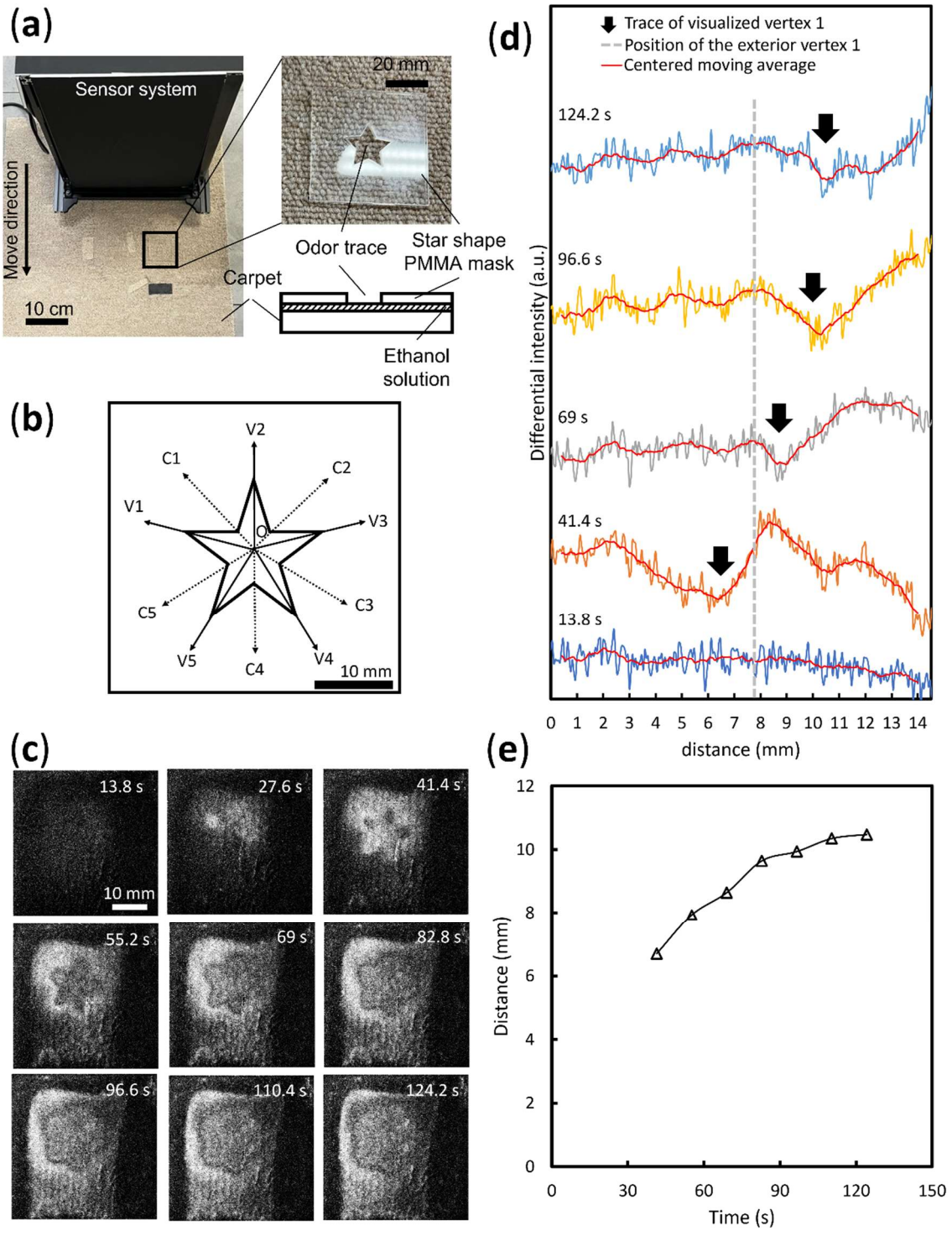

Figure 4. 6 On-ground star-shaped odor trace visualization in an indoor environment. (a) Experimental setup. (b) Directions of intensity profiles in 10 directions. (c) Differential images of the star-shaped odor trace over time. (d) Intensity profile of the line V1 at different times. (e) Position shift of the visualized vertex 1 over time.

Differential images of the visualized star shape odor trace (with the background subtracted using the first image as the reference) are shown in Figure 4.6c. For the first 13.8 seconds, notable change is not observed in the differential images. Around 27.6 seconds, there's an increase in the brightness of the image's upper half, corresponding to the star-shaped odor trace. By approximately 41.4 seconds, distinct elliptical shadows start to appear at the upper three vertices position of the star shape. At 55.2 seconds, the entire star shape becomes visible, with the interior of the star shape appearing significantly darker than its exterior, and a clear decrease in brightness at the star's edges, creating a distinct star-shaped outline. From 69 to 124.2 seconds, the entire image continues to expand outward, gradually transforming into a pentagon before ultimately becoming an irregular shape, indicating the non-symmetrical and non-uniform dispersion of the odor across the area. The rate of shape change is quicker in the V1, V2, and V3 directions, with the shape maintaining its initial form longer in other directions. The edges of the star shape in visualized images and the subsequent changes indicate the complexity of the odor diffusion process.

To more clearly show the changes and the movement of the odor trace's edge area during imaging, an intensity profile was plotted from the center O towards exterior vertex 1, over a length of approximately 15 mm (250 pixels). The intensity changes along the arrow V1 at 13.8, 41.4, 69, 96.6, and 124.2 s are shown in Figure 4.6d. The line width was adjusted to 20 pixels to reduce the influence of noise. Each arrow marker shows the position of visualized vertex 1 at different time. At 13.8 seconds, negligible intensity change is observed along arrow V1, which is consistent with the result in Figure 4.6c. By 41.4 seconds, a noticeable valley forms at roughly 6.7 mm, as highlighted by the black arrow. This valley progressively shifted outward to 8.6, 9.9, and 10.5 mm at subsequent intervals of 69, 96.6, and 124.2 seconds, respectively. At 124.2 seconds, a prolonged valley is observed between 10.5 and 12.1 mm, with two intensity decreases in the graph. This outward movement of the valley suggests a diffusion of the odor, expanding from its source.

The differential images' intensity profiles were plotted along the V1 direction within a length of 15 mm. The position of the valley was recorded every 13.8 seconds from 41.4 to 124.2 seconds. These recorded positions of valleys represent the outline of the images on the sensor substrate by the odor trace. Figure 4.6e shows the position shift of the valley corresponding to the start point of the edge of the visualized V1 over time. From 41.4 to 82.8 seconds, the valley moves from 6.7 to 9.6 mm, indicating a significant outward movement. Between 82.8 and 124.2 seconds, the shift is from 9.6 to 10. 5 mm, indicating a lesser positional change. The outline's motion speed of the visualized odor trace in

differential images is approximately 0.07 mm/s from 41.4 to 82.8 seconds and 0.02 mm/s from 82.8 to 124.2 seconds.

Figure 4.7a shows the change in intensity from the center of the star shape to each exterior vertex at 55.2 seconds. revealing a noticeable intensity change around 7.8 mm from the center, thereby highlighting the position of odor trace's edge in the images. Due to uneven diffusion in different directions, the positions of the valleys differ, but they are all near the positions of the exterior vertices. Exterior vertices 1, 2, 4, and 5 exhibit a more pronounced intensity decrease around the valleys, enhancing their visibility in the image, whereas V3 appears relatively indistinct. Figure 4.7b shows a similar result at approximately 4 mm from the center for the interior vertices of the star.

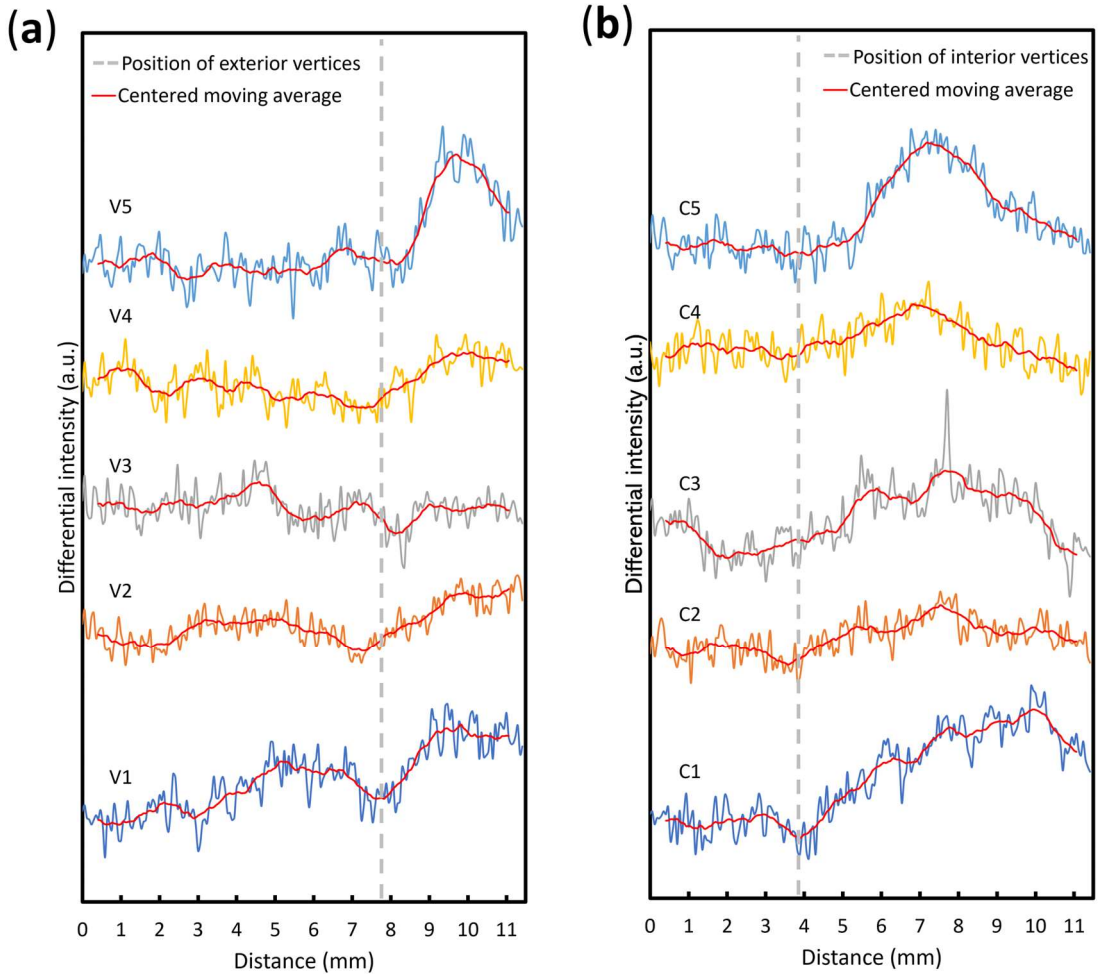

Figure 4. 7 Intensity profiles in different directions. (a) Intensity profiles along V1 to V5 at 55.2 s. The grey broken line represents the positions of the five exterior vertices. (b) Intensity profiles along C1 to C5 at 55.2 s. The grey broken line represents the positions of the five interior vertices.

The distance between the LSPR substrate and the odor trace influences image quality in various ways. In this experimental setup, the minimum achievable distance is 4-5 mm.

Due to diffusion effects, a closer distance of the LSPR substrate to the odor trace enhances the concentration difference in the local area of the substrate, resulting in clearer images. Increasing distance leads to a greater influence of external light passing through the substrate on its visualization capabilities. Due to the fast response speed of LSPR substrates (20 ms, as observed in chapter 2), time costs were not considered to be a significant factor. The differential images captured at different times can accurately represent the real-time distribution of the traces left on the substrate.

In examining the temporal changes in intensity, analyses were conducted across areas with a diameter of roughly 1.2 mm (20 pixels) at each exterior vertex. As shown in Figure 4.8, before 41.4 seconds, there is a big increase in intensity in the differential images, ranging from 29.99 to 148.97. After 55.2 seconds, the intensity in these areas remain stable (between 122.65 and 139.52). These results suggest that from approximately 55.2 seconds, the images derived from intensity variations due to the odor trace on the substrate provide comprehensive shape information about the odor trace. This method is thus considered effective for calibration in determining the optimal observation time under varying floor materials and experimental conditions.

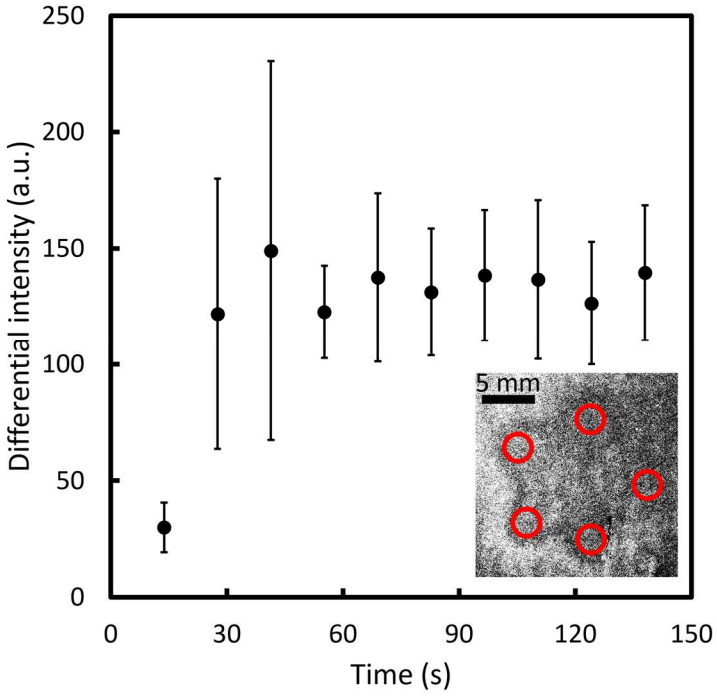

Figure 4. 8 Intensity changes at the five vertices over a period of 138 s. Red circles represent the five sampling areas of the vertices in the visualized images.

4.4. Conclusions

In this chapter, a 2D odor trace visualization system was developed based on an LSPR substrate with Au/Ag core-shell nanostructure, focusing on the observation of light scattered from the substrate's backside. This system was used to visualize on-ground odor traces.

The raw images were obtained from a close range of 4–5 mm from odor traces on the ground. After background subtraction, they showed reasonably clear brightness changes due to the volatile gas ethanol diffused from the odor trace on the sensor substrate. The differential images provide an intuitive view of the spatial distribution information (shape) of invisible odor traces and their changes over time. A comparative experiment was conducted and clearly demonstrated the ability of the LSPR substrate to capture an odor trace compared to a non-LSPR substrate under the same environmental conditions.

Indoor experiments demonstrated the system's ability to capture an odor trace with a complex shape (star shape) set in real floor environments, such as a carpet. In addition, an experimental method was developed to verify the optimal observation time for the visualization images to match the original trace shape in real-world conditions. The optimal time for capturing a star-shaped odor trace was approximately 55 s after the imaging system stopped above the odor trace in an indoor experiment. This methodology holds potential for future applications, such as in robotics, where it can be utilized to acquire spatial distribution data of odor traces at specific locations.

Reference

(1) Chen, B.; Guo, H.; Liu, C.J.; Shang, L.; Ye, X.; Chen, L.; Feng, C.H.; Hayashi, K. Molecularly imprinted sol-gel/Au@Ag core-shell nano-urchin localized surface plasmon resonance sensor designed in reflection mode for detection of organic acid vapors. Bio-sens. Bioelectron. 2020, 169, 112639. https://doi.org/10.1016/j.bios.2020.112639.

(2) Blakey, I.; Merican, Z.; Thurecht, K.J. A Method for Controlling the Aggregation of Gold Nanoparticles: Tuning of Optical and Spectroscopic Properties. Langmuir 2013, 29, 8266–8274. https://doi.org/10.1021/la401361u.

(3) Soeda, T.; Yang, Z.Y.; Sassa, F.; Hayashi, K. Gas Visualization with Photo-Induced 2d Pixel Patterned Au/Ag Core-Shell Lspr Imaging Device by Mask-Less Exposure System. In Proceedings of the 2019 20th International Conference on Solid-State Sens. Actuators Microsyst. Eurosensors XXXIII (Transducers Eurosensors XXXIII), Berlin, Germany, 23–27 June 2019; pp. 1274–1276. https://doi.org/10.1109/transducers.2019.8808591.

(4) Matsuoka, M.; Lingpu, G.; Sassa, F.; Hayashi, K. Spatiotemporal Visualization of Gases Using 2-D LSPR Gas Sensor. IEEE Sens. Lett. 2023, 7, 5000704. https://doi.org/10.1109/lsens.2023.3301847.

Chapter 5 Conclusion and prospect

5.1 Conclusion

In this research, utilizing a sensor substrate with high response speed and high spatial resolution based on the LSPR principle, an odor robot and a two-dimensional odor trace visualization system based on LSPR sensors were constructed. This enabled the real-time detection and acquisition of visual images of the spatial distribution of odor information, which was previously difficult to obtain, and established methods for information analysis.

Collecting spatiotemporal distribution information of odor traces through one-dimensional high-speed LSPR sensor with mobile robot.

Chapter 2 proposed a high speed LSPR gas sensor module utilizing the LSPR phenomenon, which converts chemical signals (odor molecules) into optical signals. The sensor module consists of an LED light source, a photodetector, and a gold nanoparticle LSPR substrate. This sensor is capable of responding to ethanol gas at high speeds, exceeding 25Hz, and can recover equally quickly after leaving the odor source. By integrating the LSPR sensor module with a mobile robot, we have achieved exploration of the spatial distribution of on-ground odor traces. Due to the sensor's rapid response, the odor distribution collected by this robot can be considered real-time spatial odor distribution information. In the test environment, even when the robot was moving at a high speed of 10 cm per second, it was still able to effectively record invisible digital spatial odor information (represented as 0 and 1 corresponding to the absence or presence of odor, respectively) that was artificially set on the ground, and translate it into readable information.

Collecting spatiotemporal distribution information of odor traces through two-dimensional LSPR sensor.

Chapter 3 proposes a two-dimensional odor trace visualization system based on an LSPR substrate with an Au/Ag core-shell nano structure. The system consists of a CCD camera and LED light source and a two-dimensional LSPR sensor substrate. This system can capture the optical absorption differences caused by the concentration distribution of odor traces on the LSPR substrate using the CCD camera, thereby recording images of the odor traces. It obtains the spatiotemporal distribution information of odor traces that change over time by differential images from the first image (background). The tens of nanometers spatial resolution of the substrate itself endows the visualization system with an extremely high spatial resolution of about tens of micrometers. Since the high response

speed of about 20 ms of the LSPR substrate has already been validated in Chapter 2, the continuous spatial distribution images of odor traces captured by the system can be considered as real-time changes of natural diffusion. Through the transmission type imaging system, we recorded visualized images of ethanol gas flow blown on the substrate. Using the reflection type imaging system, we recorded images of odor traces in the shape of the letters "Q" and "U" and the time-varying images of bar-shaped odor traces. We also defined the minimum distance required to distinguish between two odor sources as the spatial resolution of the system, which is 6 mm.

In chapter 4, we adjusted the angle of the CCD camera to prevent reflections from leaving traces in the images and fabricated an independent mobile two-dimensional imaging system. Due to the increased distance between the LSPR substrate and the odor source to 4-5mm, we conducted comparative experiments. By observing the differences in the differential images obtained under the same conditions with LSPR and non-LSPR substrates, we confirmed that the system still has the capability to clearly capture odor trace images at this distance. Furthermore, in indoor experiments, we confirmed the ability of this imaging system to capture complex odor trace images (such as stars) set on surfaces that simulate real environments, like carpets. Additionally, by comparing changes in the images with the original shape of the odor traces, we determined the optimal observation time for the visualized images, which, in this experiment, was 55 seconds after the start of capturing.

5.2 Prospect

In chapter 2, although the one-dimensional LSPR sensor module can display different signal values for various odor substances such as ethanol, acetone, and hexane, it inherently lacks selectivity. This leads to the sensor responding to all environmental changes during data collection. Imparting selectivity to the LSPR sensor using Molecularly Imprinted Polymers (MIPs) has been proven to be an effective method (1, 2). In future research, the response to specific odor substances will be enhanced by using LSPR substrates modified with MIP layers, as shown in figure 5.1. This will be achieved by employing various modifiers and multi-channel sensors to track specific odor substances. Using MIPs not only provides selectivity but also enhances the sensitivity of the sensor, as MIPs can efficiently enrich target analytes.

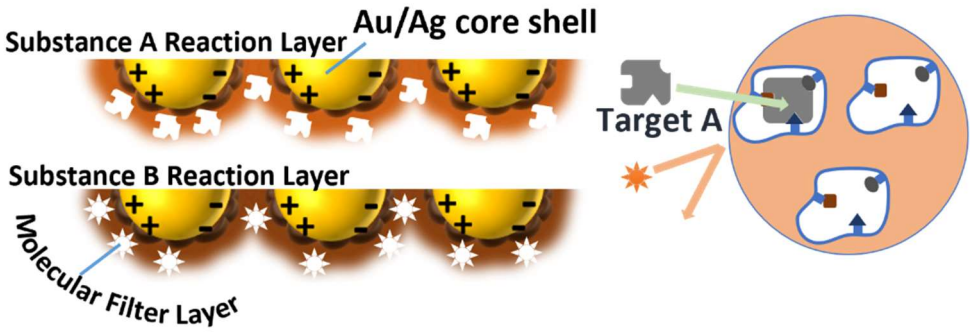

Figure 5. 1 Molecule recognizing LSPR sensor.

Pixel patterns with varying degrees of Ag nanoparticle growth on the substrate can be formed by controlling the amount of light in different pixel areas using a projector. Figure 3a shows an LSPR gas sensor substrate with a 4-segmented pixel pattern (3). The response of the 4 segmented pixels varies, and their mixture ratios to different types of gas flow can be calculated through visualized images using changes in transmitted light. Figure 3b shows a colorized result with different mixture ratios in ethanol and acetic acid. Ethanol-rich areas and acetic acid-rich areas can be clearly separated for gas type identification. The method proposed by our team is capable of identifying different gases, while maintaining the sensor's versatility without being affected by the type of the sensitive material layers. In future experiments, the ability of this method to identify odors will be verified, based on visualized images of composite odor traces on the ground obtained through reflection and scattering light.

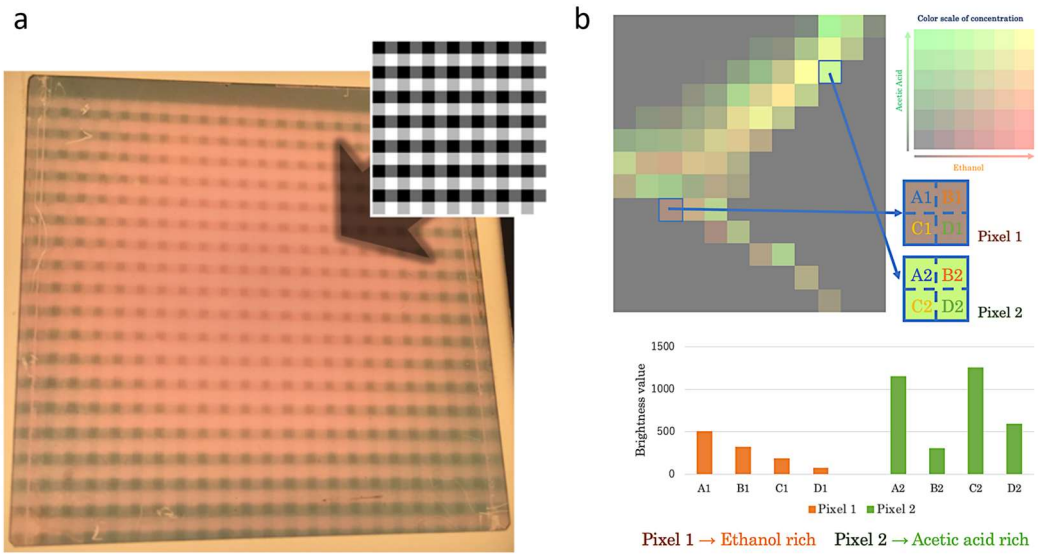

Figure 5. 2 Identification of gas types with pixelated 4-segmented LSPR sensor. [3] (a) LSPR substrate with 4-segmented pixel pattern. (b) analysis spatial gas flow distribution with 4 ch Au/Ag LSPR image sensor.

In Chapters 3 and 4, the visualization systems can clearly and noticeably record the spatiotemporal distribution information of odor traces as they change over time. However, In Chapter 3, the distance between the odor traces and the sensor substrate set on the experimental table can be very close, about 1-2 millimeters. In contrast, the visualization system for mobile robot developed in Chapter 4, the distance between the substrate and the on-ground odor substances increases to 4-5 millimeters, significantly increasing the optimal imaging time. As shown in Figure 5.3, the odor trace visualization system demonstrates changes in the differential images over time as it passes over odor traces. It's evident from the time sequence changes that there are significant imaging changes as the system pass through odor traces. However, the increased time required for these changes makes it difficult to determine the positional relationship between the visualization system and the odor traces during movement. In future research, the integration of the one-dimensional LSPR robot with the two-dimensional visualization system is planned. Leveraging the high detection speed of the one-dimensional sensor module for positioning will assist the two-dimensional visualization system in information gathering, enabling the robot to actively explore and map the distribution of odor traces.

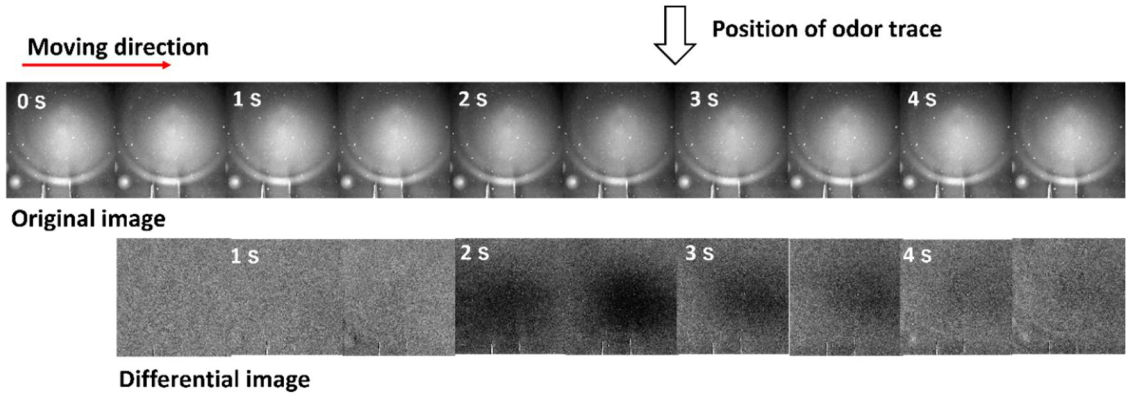

Figure 5. 3 image changes passing through odor trace.

Reference

(1) Chen, B.; Liu, C. J.; Sun, X.; Hayashi, K.; Ieee. Molecularly Imprinted Polymer Coated Au Nanoparticle Sensor for α-pinene Vapor Detection. *2013 Ieee Sensors* **2013**, 117-120.

(2) Guerreiro, J. R. L.; Bochenkov, V. E.; Runager, K.; Aslan, H.; Dong, M. D.; Enghild, J. J.; De Freitas, V.; Sales, M. G. F.; Sutherland, D. S. Molecular Imprinting of Complex Matrices at Localized Surface Plasmon Resonance Biosensors for Screening of Global Interactions of Polyphenols and Proteins. Acs Sensors 2016, 1 (3), 258-264. DOI: 10.1021/acssensors.5b00054.

(3) Soeda, T.; Yang, Z.Y.; Sassa, F.; Hayashi, K. Gas Visualization with Photo-Induced 2d Pixel Patterned Au/Ag Core-Shell Lspr Imaging Device by Mask-Less Exposure System. In Proceedings of the 2019 20th International Conference on Solid-State Sens. Actuators Microsyst. Eurosensors XXXIII (Transducers Eurosensors XXXIII), Berlin, Germany, 23–27 June 2019; pp. 1274–1276. https://doi.org/10.1109/transducers.2019.8808591.

Acknowledgement

I have been fortunate enough to receive invaluable assistance and support from many people during my research life at Kyushu University. Beginning at the end of my first doctoral year, I faced some physical and mental discomfort. Their help was essential in enabling me to complete my studies.

I would like to express my deepest gratitude to my supervisor, Prof. Kenshi Hayashi, for his unwavering support and guidance throughout the course of this research. His expertise and insights have been invaluable, and his encouragement was a constant source of motivation.

I would like to extend my sincere appreciation to Prof. Fumihiro Sassa, who gives me precious advice in my research life. His endless patience is a great help during my experiment, discussion, article writing, and submission.

I am also deeply grateful to the members of my thesis committee, (Prof. Yuji Oki as the chief examiner), whose valuable feedback and constructive criticism greatly improved the quality of this work.

I extend my sincere thanks to Mr. Hao Guo, whose shared insights and discussions greatly enriched this research. Similarly, I am deeply grateful to Miss Shiyi Zhang for her invaluable assistance in developing the tools essential for the experiments.

I would like to thank Dr. Midori Watanabe, Dr. Hirotaka Yoshioka, Mr Takaaki Soeda in Hayashi Lab for their help in my experiment.

I would like to thank secretaries in Hayashi Lab (Ms. Maiko Moribe, Mr. Shigeru Kaneko, Ms. Yuukou Saruwatari), for their help in my study and daily life.

Many thanks to all friends in Hayashi Lab for their friendship during my life in Japan.

I would like to extend special thanks again to Prof. Fumihiro Sassa for his invaluable help during a particularly challenging time when I was struggled with mental problem.

My heartfelt appreciation goes to my family, for their love, understanding, and patience throughout my doctoral journey. Their unwavering faith in me has been a constant source of strength.